Tsunami wave run-up load reduction inside a building array

Joaquin P. Moris, Andrew B. Kennedy, Joannes J. Westerink

PII: S0378-3839(21)00070-3

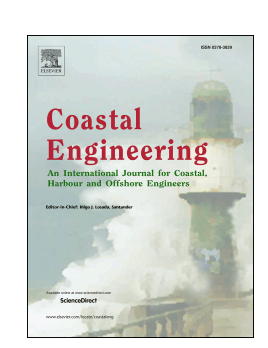
DOI: https://doi.org/10.1016/j.coastaleng.2021.103910

Reference: CENG 103910

To appear in: Coastal Engineering

Received Date: 16 October 2020

Revised Date: 1 April 2021 Accepted Date: 16 April 2021



Please cite this article as: Moris, J.P., Kennedy, A.B., Westerink, J.J., Tsunami wave run-up load reduction inside a building array, *Coastal Engineering*, https://doi.org/10.1016/j.coastaleng.2021.103910.

This is a PDF file of an article that has undergone enhancements after acceptance, such as the addition of a cover page and metadata, and formatting for readability, but it is not yet the definitive version of record. This version will undergo additional copyediting, typesetting and review before it is published in its final form, but we are providing this version to give early visibility of the article. Please note that, during the production process, errors may be discovered which could affect the content, and all legal disclaimers that apply to the journal pertain.

© 2021 Elsevier B.V. All rights reserved.

CRediT authorship contribution statement

Joaquin P. Moris: Conceptualization, Methodology, Software, Validation, Formal analysis, Investigation, Writing - Original Draft, Visualization.

Andrew B. Kennedy: Conceptualization, Methodology, Investigation, Resources, Writing - Review Editing, Supervision, Project administration, Funding acquisition.

Joannes J. Westerink: Conceptualization, Resources, Writing - Review Editing, Supervision.

Highlights

Tsunami wave run-up load reduction inside a building array

Joaquin P. Moris, Andrew B. Kennedy, Joannes J. Westerink

- The effect of a building array on maximum run-up loads was studied.
- Maximum wave run-up loads decrease as more rows of buildings are providing shelter.
- Load Reduction Factors (LRF) are defined to evaluate the run-up load reduction.
- The inundation depth, velocity, and momentum flux magnitudes inside the building array are larger than bare earth values.

Tsunami wave run-up load reduction inside a building array

Joaquin P. Moris^{a,*}, Andrew B. Kennedy^a and Joannes J. Westerink^a

^aUniversity of Notre Dame, 156 Fitzpatrick Hall, Notre Dame, IN 46556, USA

ARTICLE INFO

Keywords:
Run-up wave loading
Tsunami
Sheltering
Load reduction
Building array
CFD
olaFlow

ABSTRACT

The influence of a building array on tsunami-driven run-up loads is studied through laboratory experiments and Computational Fluid Dynamics (CFD) simulations. Results show that the number of rows of buildings providing shelter is an explanatory variable for the maximum wave run-up load reduction. Load Reduction Factors (LRF) are defined, with values monotonically decreasing as the number of rows providing shelter increases. The effect of the building array on maximum inundation levels, maximum cross-shore velocity, and maximum momentum flux is studied, finding that these hydrodynamics properties have larger magnitudes when compared to bare earth values. A brief discussion about the effect of the cross-shore distance between rows, the width of the structures in the frontmost row, and the offset between rows is presented. Under the wave conditions and the geometry tested, maximum wave loading is decreased up to about 4 times when 4 or more rows are providing shelter, with most of the load reduction taking place in the first 4 rows. When more than 4 rows are providing shelter to a structure of interest, Load Reduction Factors decrease weakly with the number of rows providing shelter. Although the present analysis has limitations in terms of geometry and wave conditions and more tests have to be conducted to draw conclusions for a wider range of conditions, it shows experimental and numerical evidence that maximum wave loading on structures can be strongly affected when they are part of a building array.

1. Introduction

Tsunami events in developed regions are a major coastal hazard, repeatedly causing loss of life and damage to public and private infrastructure. The 2004 Indian Ocean Tsunami left 350,000 people reported killed or missing and an estimated economic damage of 4.5 billion US dollars (Athukorala and Resosudarmo, 2005). As a consequence of the 2011 Great East Japan earthquake and tsunami, 19,334 people were reported dead or missing (Suppasri et al., 2012) with a damage exceeding 235 billion US dollars (Davis et al., 2012). The 2010 Chilean Tsunami accounted for 124 victims (Fritz et al., 2011) and a total economic loss estimated at 30 billion US dollars (Khew et al., 2015). Climate change and the associated projected sea level rise is expected to move shorelines inland, increasing the exposure of coastal communities to coastal hazards (Kopp et al., 2014). In addition to the increase in ocean water levels, global population is expected to increase (Angel et al.,

^{*}Corresponding author

[≥] jmorisba@nd.edu (J.P. Moris); andrew.kennedy@nd.edu (A.B. Kennedy); jjw@nd.edu (J.J. Westerink) ORCID(s): 0000-0001-9736-0237 (J.P. Moris); 0000-0002-7254-1346 (A.B. Kennedy)

2011) and coastal communities are likely to keep expanding (McGranahan et al., 2007), which will result in more people and infrastructure being exposed to tsunami hazards.

To reduce the number of victims and the economic damage caused by these events, it is necessary to improve the resiliency of coastal communities and design standards by understanding and estimating the physical impact of tsunami-driven flows in developed regions. A direct understanding of the impact of tsunami flows comes from field surveys. Observations from field surveys are useful to obtain data of post-event damage, flow depth, and maximum run-up heights (e.g. Fritz et al., 2011; Suppasri et al., 2012). Data from post-event damage on buildings is crucial to improve the resiliency of coastal communities because it can be used to validate tsunami vulnerability models (Dall'Osso et al., 2010; Omira et al., 2010). Likewise, flow depth and maximum run-up data from tsunami field surveys are used to validate tsunami numerical models (e.g. Lynett et al., 2003; Nicolsky et al., 2011). Unfortunately, in a post-event survey it is not possible to get direct measurements of tsunami flow velocities, pressures, and wave loading on structures: all essential variables for characterizing coastal processes during inundation. This knowledge is fundamental to reduce coastal damage by improving coastal urban planning and tsunami load estimates in design standards.

1.1. Wave loading on single structures

Fundamental studies of the evolution of the pressure, and the resulting wave loading on single isolated structures due to wave action on the coast have been addressed through laboratory experiments for several decades. Oumeraci et al. (1993) gave perhaps the first comprehensive experimental study in which measurements of pressure, forces and video records of the wave impact on a coastal vertical structure were recorded simultaneously for several breaker types. Based on video observations and pressure measurements it was found that for similar wave conditions, the resulting wave loading peak on the wall depends primarily on the position of the breaking point with respect to the front of the wall. When plunging breaking took place near the wall, a sharp wave loading peak of very short duration occurred, followed by a load lower in magnitude, but lasting longer. The magnitude of the sharp peak has been found to be inversely proportional to its rising time of the peak, i.e. greater impact pressures have shorter duration, and vice versa (Kirkgöz, 1995). When breaking occurred further from the wall or the wave was non-breaking, peaks had lower magnitude but longer duration. Loads from plunging waves breaking near or on a structure are defined as impact loads and loads from already breaking waves or non-breaking waves are defined as pulsating loads (Klammer et al., 1996).

Significant attention has been given to impact loads in recent years because their magnitudes can exceed by several times their corresponding pulsating loads (Hattori et al., 1994; Chan et al., 1995; Cuomo et al., 2010). Impact loads are a highly complex process in which water, air and the structure interact with each other in a very short period of time. The entrapped air located below the wave crest may result in pressure oscillations with the resonant frequency of pulsating air pockets, reaching even negative pressure peaks (Bullock et al., 2007; Kihara et al., 2015; Lugni et al., 2006). Despite the high complexity and experimental variability of impact loads on vertical structures, predictive equations have been developed to estimate their maximum values (Klammer et al., 1996; Cuomo et al., 2010). Although maximum values of pulsating loads are not as high as impact loads, their duration is much longer. Tsunamis are composed of a series of waves with very long wave periods, therefore their associated wave loading acts for a long period of time, resembling

a pulsating load rather than an impact load. The first wave from the series will likely break before reaching the shoreline, encountering coastal structures on dry land. Once the first wave inundates land, the next series of waves will encounter the structures over a flooded bed. Therefore, pulsating wave loading has been investigated for both dry and wet bed conditions (Goda, 1974; Ramsden, 1996; Cuomo et al., 2010).

Pulsating loads can be separated into an initially transient part and a following quasi-static component. The transient part usually contains the peak load, which should not be confused with an impact load. Peak transient loads have been found to be reasonably well predicted using linear momentum equations (Linton et al., 2013; Robertson et al., 2013). Pulsating loads are often estimated as a drag force using a constant drag coefficient. Xie and Chu (2019) through numerical experiments found that equilibrium drag coefficients are within the range of current design guidelines, but peak drag coefficients associated with initial wave impacts were found larger than equilibrium drag coefficients, which should not be ignored in structural design. The orientation of the structure with respect to the flow direction can also have an effect on the magnitude of the drag coefficient (Shafiei et al., 2016).

1.2. The effect of building arrays on wave loading

1.2.1. Building array consideration in current guidelines

Hydrodynamic tsunami loads are usually estimated as a drag force, proportional to the maximum momentum flux (Yeh, 2006). Current design guidelines in the USA use this estimation to evaluate tsunami loads on vertical structures with a safety or an importance factor (ASCE7-16, 2017; FEMA, 2011, 2012; CCH, 2000). Japanese standards use an equivalent hydrostatic pressure to estimate lateral hydrodynamic loads with a ratio of design height to inundation height up to 3 (Fukuyama et al., 2011). The above mentioned studies and design standards are primarily focused on wave loading on single structures, without considering the interaction of the flow with other structures. However, the presence of a building array can considerably influence wave loading. The term "building array" in this paper refers to a group of structures located in the inundation zone that interacts with the flow, influencing the hydrodynamics and loads on a structure of interest. ASCE7-16 (2017), in the commentary section, offers some limited guidelines on the influence of a building array in the magnitude of the tsunami flow velocity and forces. Under particular conditions, a building array can induce channelized flow conditions resulting in flow amplification factors, which can be applied at the engineer's judgment. ASCE7-16 (2017) does not allow a reduction in flow velocity or loads when a building array provides shielding.

1.2.2. Shielding effect in field surveys and vulnerability models

The 2006 Java tsunami field observation work reported by Reese et al. (2007) shows that in the town of Pangandaran, although there was total damage to the shops along the beach, the tsunami waves did not seriously damage structures further inland because more robust commercial buildings close to the coast protected the inland urban area. Leone et al. (2011) showed in a study area in the city of Banda Aceh in Indonesia that a well-made reinforced concrete mosque was able to provide sheltering to a weaker brick building, even though the waves were up to 14 m high. Albeit not from a tsunami survey, Hatzikyriakou et al. (2016) identified two adjacent regions that experienced considerably different foundation damage on residential structures from Hurricane Sandy in Ortley Beach, NJ, USA. Region A did not have large structures in the oceanfront, whereas Region B had three large oceanfront structures. The foundation damage on the residential structures of Region B

Journal Pre-proof vvave run-up load reduction inside a building array

was found to be markedly less than in Region A due to the presence of the large structures in front of the urban array. It is believed that the large oceanfront structures acted as breakwaters, reducing the surge loads on the inland structures during the inundation event.

Sheltering induced from the presence of a building array has been used as a parameter in the development of probability functions of level of damage in structures after an inundation event. Tomiczek et al. (2017) assigned a Shielding Parameter (SP) to each house surveyed by Hatzikyriakou et al. (2016), which was used in a multi-variable regression model to develop Damage State (DS) functions. A reasonable agreement between the post-storm SP and DS was obtained. Furthermore, SP along with the water velocity were found to be the two best explanatory variables for DS. Although, the SP was developed for hurricane damage, it still shows that damage from waves can be mitigated by the presence of a building array. The PTVA-3 model (Papathoma Tsunami Vulnerability Assessment, version 3) is a tool that provides an assessment of the tsunami vulnerability to individual buildings (Dall'Osso et al., 2009). The PTVA-3 model uses as one of its independent variables a protection factor based on the row location in a building array. The PTVA-3 model validations presented in Dall'Osso et al. (2010, 2016); Izquierdo et al. (2018) show that the vulnerability under tsunami events depends on the row location within the building array in the coast. Reese et al. (2011) also found that shielding is an explanatory variable in describing the level of observed damage in Samoa and American Samoa after the 2009 South Pacific tsunami, finding that the probability of exceeding the most severe damage states, is considerably less if shielding is present.

1.2.3. Shielding effect in wave hydrodynamics and wave loading inside building arrays

Tsunami-driven flows increase their complexity when interacting with building arrays, affecting the hydrodynamics of the flow. Rueben et al. (2011) used optical measurements in a physical tsunami experiment to find that the presence of macro-roughness elements can reduce the propagation speed of the tsunami bore in residential areas up to 40% on average. Park et al. (2013) shows that the momentum flux along a cross-shore residential street is reduced as the bore moves inland. Results from Park et al. (2013) using the COULWAVE Boussinesq model (Lynett et al., 2002) show that when including building geometries in the domain, maximum values of momentum flux inside the building array can be overestimated between 60% and 260%, presenting a challenge for current depth averaged models to predict the hydrodynamics inside building arrays. Goseberg (2013) found that maximum tsunami run-up on a beach slope can be reduced if a building array is present, with an increase in the reduction as the buildings in the array are closer together.

Studies of wave loading shielding in building arrays have been conducted in recent years, yet a universal shielding law remains unresolved due to the large number of independent variables. In general, depending on the location of each structure belonging to the building arrangement, maximum loading magnitudes can increase or decrease when compared to unshielded conditions. For instance, Simamora et al. (2007) studied the decrease in wave loading on the structures of a regularly spaced building array through a set of laboratory experiments in an idealized building grid with 4 rows of structures on an initially dry flat test section. Their results show that wave loading peaks decrease as the number of sheltering buildings increases. The maximum wave loading recorded in the Simamora et al. (2007) experiments was reasonably estimated by standard engineering formulae on unobstructed structures; however, when the building array is placed in front a structure of interest, standard engineering formulae overestimate the wave loading peaks. Re-

sults from a multiphase Navier-Stokes model (Nakamura et al., 2010) and a Smoothed Particle Hydrodynamics (SPH) and a Discrete Element Method (DEM) model (Ardianti et al., 2015) show a similar shielding effect. Thomas et al. (2015) conducted a laboratory experiment where wave loading was recorded on an instrumented specimen. In front of the specimen, two buildings with a gap between them were placed directly in front of the instrumented specimen. It was found that depending on the location of the two front buildings, maximum loads could be reduced up to 40% or even amplified by about 40%. Similar force amplification values were also found by Nouri et al. (2010). Tomiczek et al. (2016) analyzed the change in maximum pressure on structures inside a 3 x 3 building array, finding that maximum pressure can be reduced between 40% and 70%, when compared to unsheltered conditions. Tomiczek et al. (2016) also found that as the distance between the buildings of the array decreases, the reduction in maximum pressure increases. Yang et al. (2018) conducted Computational Fluid Dynamics (CFD) wave simulations with two buildings in a flat test section, where the effect of (1) the front building width and (2) the distance between the front and the back building on the wave loading was studied. Their results show that the reduction or increase in wave loading when compared to undisturbed conditions is very sensitive to the variables studied. Depending on the relative size and distance between of the two buildings, maximum wave loads can be reduced or amplified. Two separate studies (Sogut et al., 2019; Moon et al., 2019) tested different urban arrays. It was found that maximum wave loading is amplified when a gap is located in front of an instrumented specimen, but when a structure of the building array is placed in front of the instrumented specimen, the maximum load is reduced when compared to unobstructed conditions.

1.3. Knowledge gaps and aim of this study

Previous studies of wave loading on building arrays have been studied in arrays with 2 rows (Thomas et al., 2015; Yang et al., 2018; Sogut et al., 2019), 3 rows (Ardianti et al., 2015; Tomiczek et al., 2016), and up to 4 rows (Simamora et al., 2007). In this work, through experimental laboratory tests and Computer Fluid Dynamics (CFD) simulations, we analyzed the effect of the presence of a building array on wave loading extending the number of rows, ranging from 1 up to 10 rows. The effect of the cross-shore distance between rows, the width of the structures in the frontmost row, and the offset between rows is briefly discussed. The change in maximum inundation depth, cross-shore velocity, and cross-shore momentum flux inside the building array is also examined.

This work is organized as follows: section 2 presents the OpenFOAM®-based olaFlow numerical model used in this study. Section 3 presents the details of the laboratory data used and a validation of the numerical model. The methodology of this study is presented in Section 4. Results and discussions of the effect of the building array on the loads and hydrodynamics are presented in Section 5 and 6, respectively. Finally, conclusions are presented in section 7.

2. Numerical methods

Numerical simulations were performed using olaFlow, a development derived from the IH-FOAM model (Higuera, 2015) based on the numerical model OpenFOAM®. olaFlow can solve the Navier Stokes equations for two incompressible phases and includes several options for wave generation and wave absorption, which replicate the wave physics in many coastal processes in both the laboratory and the field. In this work olaFlow was used with OpenFOAM® v1806.

2.1. Governing Equations

Fluid motion was simulated using the incompressible Reynolds averaged Navier Stokes equations (RANS), which are time-averaged equations of motion for fluid flow. The governing RANS equations are presented in Eq. (1) and Eq. (2)

$$\nabla \cdot (\rho \mathbf{U}) = 0 \tag{1}$$

$$\frac{\partial \rho \mathbf{U}}{\partial t} + \nabla \cdot (\rho \mathbf{U} \mathbf{U}) = -\nabla p^* - g \mathbf{X} \nabla \rho + \nabla (\mu_{\text{eff}} \nabla \mathbf{U}) + \mathbf{F}_{ST}$$
 (2)

where U is the velocity vector, ρ is the density, $\mu_{\rm eff}$ is the effective dynamic viscosity, p^* is the pressure in excess of the hydrostatic pressure ($p^* = p - \rho g X$), p is the total pressure, g is the gravitational acceleration, X is the position vector, and F_{ST} is the surface tension force. The effective dynamic viscosity $\mu_{\rm eff}$ is defined in equation (3)

$$\mu_{\text{eff}} = \mu + \mu_{\text{T}} \tag{3}$$

where μ is defined in equation (6) and μ_T depends on the type of turbulence model. In this work both the k- ϵ (Launder and Spalding, 1974) and the k- ω SST (Menter et al., 2003) turbulence models were considered with default parameters. In our numerical experiments there were no significant differences in the results obtained with both models. The results shown in this paper were computed using the k- ω SST turbulence model. Although recent developments in turbulence modeling have shown that the closure turbulence models used in this work are unconditionally unstable (Larsen and Fuhrman, 2018), this issue seems to affect the transformation of waves over a long duration $(t/T \gg 1)$, which is not the case of the single-waves that were simulated in this work.

RANS equations were solved on an unstructured mesh using a finite volume method for two flow phases: air and water. The volume of fluid (VOF) method is used to track and locate the free surface and to solve the momentum equation when air, water, or a mixture of both are present in the computational cell. The VOF method is based on a fraction function α , a scalar defined for each computational cell as the ratio of the volume of water to the volume of the cell. Therefore, if $\alpha = 1$ the cell is full of water, if $\alpha = 0$ the cell is full of air, and if $0 < \alpha < 1$ the cell contains both water and air and it is considered part of the interface between both fluids. The value of α propagates according to the transport equation (4).

$$\frac{\partial \alpha}{\partial t} + \nabla \cdot (\alpha \ \mathbf{U}) + \nabla \cdot (\alpha \ (1 - \alpha) \ \mathbf{U}_r) = 0 \tag{4}$$

The term $\nabla \cdot (\alpha \ (1-\alpha) \ U_r)$ in the LHS of equation (4) is an extra artificial compression term to ensure the necessary compression at the interface to keep α bounded between 0 and 1 (Rusche, 2002). This term is different from zero only at the interface due to the $\alpha(1-\alpha)$ factor, and U_r is a velocity field used to compress the interface and has a magnitude of $|U_r| = \min\{c_\alpha |U|, \max(|U|)\}$, where c_α is a compression coefficient specified by the user, which has a default value of 1, but can be greater than 1 to increase the compression of the interface (Higuera et al., 2013).

The local density ρ and the local viscosity μ of the fluid are computed according to the equations (5) and (6), respectively.

$$\rho = \alpha \rho_{\text{air}} + (1 - \alpha) \rho_{\text{water}} \tag{5}$$

$$\mu = \alpha \mu_{\text{air}} + (1 - \alpha) \mu_{\text{water}} \tag{6}$$

where $\rho_{\rm air}$ is the density of the air, $\rho_{\rm water}$ is the density of the water, $\mu_{\rm air}$ is the viscosity of the air, $\mu_{\rm water}$ is the viscosity of the water.

Surface tension is approximated using a Continuum Surface Force (CSF) model, which computes the surface tension effect for a finite thickness interface (Brackbill et al., 1992) following Eq. (7)

$$F_{ST} \approx \sigma \kappa \nabla \alpha$$
 (7)

where σ is the surface tension coefficient, and κ is the curvature of the interface given by $\kappa = \nabla \cdot (\nabla \alpha / |\nabla \alpha|)$. We use the ratio of gravitational and surface tension forces known as the Bond Number (Bo = $\Delta \rho g L_c^2 / \sigma$) to find if surface tension is important in this study, where $\Delta \rho = 999 \text{ kg/m}^3$ is the difference in density of water and air, $g = 9.81 \text{ m/s}^2$, $\sigma = 0.07 \text{ N/m}$, and L_c is a characteristic length which in this case we consider the width of the structures, thus $L_c = 0.4 \text{ m}$. This gives Bo = $2.24 \cdot 10^4 \gg 1$, therefore the flow is unaffected by surface tension effects.

2.2. Numerical Solver

The PIMPLE algorithm is the numerical solver used to solve the RANS equations, which is an algorithm based on two methods that solve the pressure-velocity coupling: SIMPLE (Semi Implicit Method for Pressure Linked Equations) and PISO (Pressure Implicit with Splitting of Operators) (Versteeg and Malalasekera, 2007). Both algorithms solve the pressure and the velocity components by a guess and correct procedure. The pressure is initially guessed and it is used to estimate the velocity components which are then corrected until convergence in both the mass and momentum equation is achieved.

2.3. Boundary Conditions

One of the advantages of using the olaFlow model is that it includes options to generate several different types of wave conditions. In this study, the solitary wave generation and the piston-type boundary condition were used for model validation, and the piston-type boundary condition was used in the rest of this study. A description of each of the wave generation methods can be found in Higuera (2015).

3. Model Validation

OpenFOAM-based numerical model IHFOAM and olaFlow have been recently used for computing and analyzing wave loads in coastal structures, obtaining good agreement with experimental data (e.g. Douglas and Nistor, 2015; Park et al., 2018; González-Cao et al., 2019; Huang et al., 2018; Arabi et al., 2019). However, for any particular analysis using a CFD model a proper spatiotemporal resolution must be chosen that achieves a result in a reasonable computation time without sacrificing quality. For this study, we validated the model by sequentially increasing the resolution from a coarse to a fine mesh until both convergence and good agreement against data from two different laboratory experiments was achieved. The model was validated using data from laboratory experiments conducted in Kyoto University's Hybrid Tsunami Open Flume in Ujigawa (HyTOFU) Laboratory (Tomiczek et al., 2016) and, as a part of this study, in Oregon State University (OSU) Directional Wave Basin.

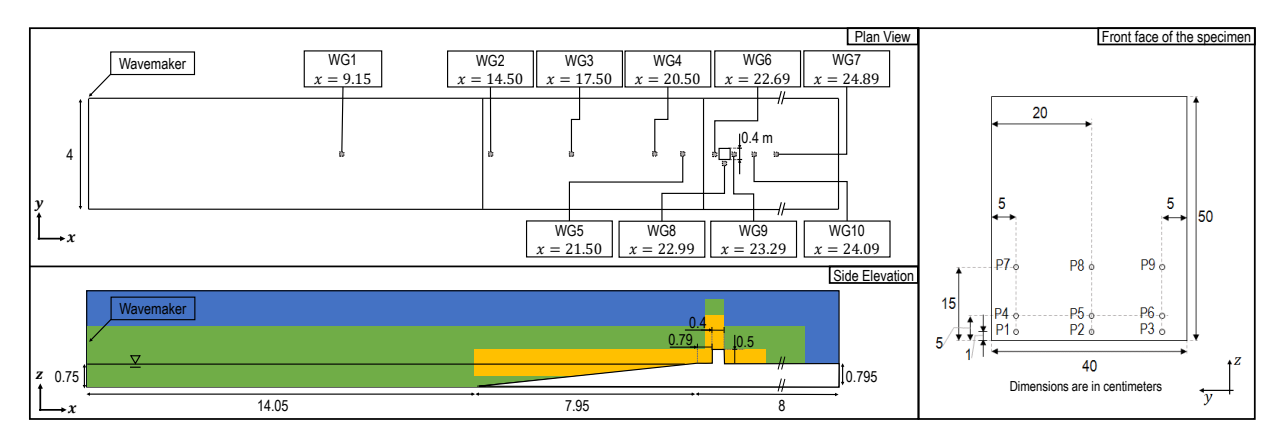


Figure 1: Left: plan view and side elevation of the HyTOFU Experimental set up with the location of the wave gauges. Right: front face of the specimen with the location of the pressure gauges.

3.1. Kyoto University's Hybrid Tsunami Open Flume (HyTOFU) Experiment 3.1.1. Description of the HyTOFU experiment

Experiments were conducted in a 45 m long, 4 m wide, and 2 m deep flume. The bottom profile consisted in a flat bed of a length of 14.05 m, followed by a 1:10 constant slope beach with horizontal length 7.95 m, and a 8 m flat test section at an elevation of 0.795 m. A single specimen instrumented with pressure gauges was placed in the test section. Plan and side views of the flume are shown in Figure 1. Wave loading on the specimen was driven by a combination of solitary waves of different heights that were generated by a mechanical piston, and a constant flow that was generated with pumps discharging water at the initial 14.05 m flat bed section. Different combinations of solitary waves and currents were tested ranging from only strong current to a nearly pure 40 cm solitary wave. We used the nearly pure 40 cm solitary wave to validate the model, because in this paper we are interested in wave driven loading. Free surface elevation was measured in 10 different locations (Figure 1) using resistance-type Wave Gauges (WG). The specimen was fixed to the test section and it was instrumented with pressure sensors at elevations of 0.01 m, 0.05 m, and 0.15 m above the test bed as shown in Figure 1. Pressure measurements were recorded at 200 Hz. For a full description of the experiments the reader is referred to Tomiczek et al. (2016).

3.1.2. Numerical Setup

The geometry in the numerical setup matched the physical setup. The bottom profile was modelled using wall functions and a no-slip condition to represent the concrete and the lateral walls were modelled using a slip condition to represent the glass on the sides. A 40 cm solitary wave over a water level of 0.75 m was generated using the solitary wave boundary condition in olaFlow.

An unstructured mesh with 3 different resolution regions (Figure A1) was used. In general, low resolution was placed where only air was present ($\alpha = 0$), high resolution was placed in the vicinity of water ($\alpha = 1$) and water-air interface ($\alpha = 0.5$) mesh regions, and the highest resolution was placed at the breaking location and in the vicinity of the specimen mesh regions. This allowed us to obtain results in a reasonable time, without sacrificing accuracy. We started from a very coarse mesh, increasing the grid resolution up to a point where both grid convergence and good agreement with the experimental data were found. The final three final meshes obtained from this procedure

are presented in this paper, which are designated coarse, mid, and fine. Details about the different unstructured meshes are found in Table A.1 in the Appendix A.

3.1.3. Model performance

As shown in Figure 2, the free surface elevation from the model shows excellent agreement with the WG measurements in the initial flat and sloping sections both before (WG1, WG2, WG3), and after wave breaking (WG4, WG5). WG6 did not record data properly, thus we could not assess the representation of the free surface elevation in front of the specimen. However, WG measurements in the test section indicate good agreement, except for the peak overprediction at WG8 which was located to the side of the specimen. The disagreement at location WG8 could be explained by differences in water splashing at the peak. In the laboratory η is measured as the closest body of water from above, whereas in the post-processing of the simulation results η is obtained by vertically integrating the fraction of water α as $\int_0^\infty \alpha dz$, which does not necessarily capture water splashing in any disconnected column of water. Away from the peak, the agreement at WG8 is very good. The agreement behind the specimen (WG9) did not match the data as well as the other WGs, however the free surface elevation magnitude is very low at these location, which makes it difficult for the model to capture this accurately. Downstream from the specimen (WG7 and WG10) the free surface elevation shows good agreement, although the exact peak is slightly shifted.

The temporal evolution of the pressure before, during and after the peak values shows very good agreement with the data recorded from the sensors in the front face of the specimen (Figure 2). However, at the location of the sensors placed 1 cm above the test bed (P1, P2, and P3), the model did not capture peak values of the pressure as accurately as the sensors placed 5 cm and 15 cm above the flat bed. This could be due to the proximity of the pressure sensor to the flat bed, where in the simulation it is only one computational cell away from the flat bed (dz = 1 cm), which could lower the accuracy of the results for those particular points. Another reason for the discrepancy of the peaks in the bottom pressure sensors is that the low frequency of the pressure measurements (200 Hz) could have been not enough to capture the rise of the pressure during a very short period of time. As mentioned by Cuomo et al. (2010), sampling frequencies lower than 1,000 Hz could result in a pressure peak reduction of almost 20%. We acknowledge this issue as a limitation for validating the instantaneous pressure given by the model at the bottom pressure sensors. The pressure peaks in the sensors located 15 cm above the flat bed (P7, P8, and P9) were not properly captured by the model when using the coarse mesh, however when the mid and fine mesh are used, the pressure peaks show good agreement with the experimental data.

3.2. Oregon State University Experimental Data

3.2.1. Description of the OSU experiments

A set of experiments involving different institutions were conducted at Oregon State University (OSU) in the O.H. Hinsdale Wave Research Laboratory Directional Wave Basin (DWB). The experiments aimed to investigate waves and debris damage, the effect of a building array, a partial seawall, and vegetation on an idealized coastal development. As a part of this study, the effect of a building array on tsunami-like waves run-up hydrodynamics and wave loading is investigated. A 10 m wide concrete beach laterally constrained by inner lateral walls was constructed inside the DWB (Figures 4 and 5). To reduce wave reflection in the basin, breakwaters were constructed to serve as wave dissipators on both sides outside of the concrete beach (Figure 5, in yellow). Wave generation was initiated with a piston-type wavemaker. In the first 12.5 m, waves propagated over

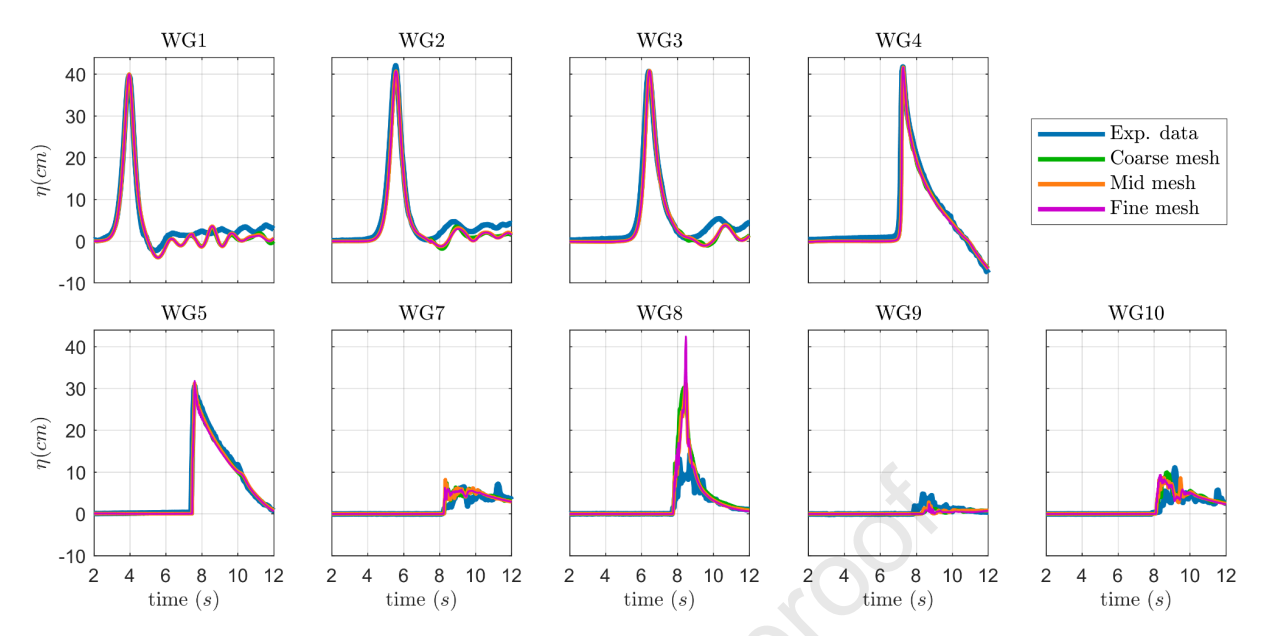


Figure 2: Free surface elevation comparison between the HyTOFU experimental data and the numerical model, including the three meshes tested.

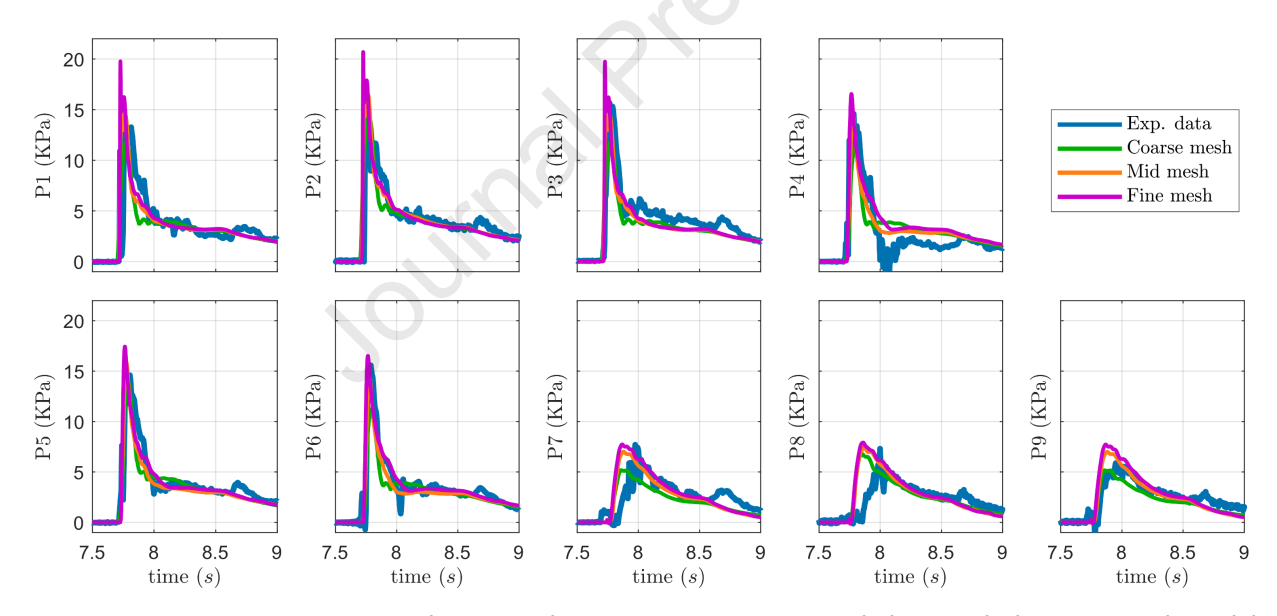


Figure 3: Pressure comparison between the HyTOFU experimental data and the numerical model, including the three meshes tested.

a flat bathymetry then to the concrete beach: first the wave shoaled over a 20 m long, 1 m height, 1:20 constant slope, and secondly on a 10 m long, 1 m elevated dry flat test section. After the test section the water flow was deposited in a 1 m deep reservoir. The initial water depth was 0.98 m, which gives 0.02 m of difference between the flat bed and the initial water level. On the test section, a 10 x 10 building array of 100 idealized structures was placed representing a coastal developed region (Figure 4 and 5). In this paper we use the term "row" to indicate the cross-shore location of

the structures, with row 1 referring to the group of structures located closest to the beach slope, and row 10 as the group of structures located closest to the back reservoir. The structures used were all 0.4 m cubes. From edge to edge, they were spaced 0.6 m in the along-shore direction and 0.4 m in the cross-shore direction. The distance from the front face of the first row of structures to the beginning of the test section was 1.6 m. Tsunami-like waves were generated using a wavemaker displacement that followed an error function (e.g. Park et al., 2019). The displacement over time of the wavemaker piston during the wave generation phase was given by

$$S(t) = 1 + \text{erf}(t/S_f - 2.871)$$
 (8)

where S(t) is the displacement of the board in meters, t is time, and S_t is a scale factor. The scale factor S_f controls how quickly the piston is displaced over the 2 m paddle stroke. The lower the value of S_f , the faster the piston. A value of $S_f = 2.5$ s was used for model validation. Wave loading was recorded in eight (8) aluminium-built structures recording at 1000 Hz: five (5) structures, located in rows 1 to 5, were instrumented with in-line load cells recording loads in the direction of wave propagation; two (2) structures, both located in row 1, were instrumented with 6 vertically spaced pressure sensors along the structure centerline; and one (1) structure in row 1 was instrumented with a six-degree of freedom load cell. The rest of the structures (92) were built with concrete blocks and were not instrumented. This paper focuses on the change of the loads at different rows, therefore in this study the recordings from the 5 in-line load cells were used. Free surface elevation was recorded in the 1:20 slope using nine resistance-type wave gauges (WG). Five ultrasonic wave gauges (USWG) recorded the free surface elevation in the test section and four Acoustic Doppler Velocimeters (ADV) recorded the instantaneous velocity 2 cm above the bottom in the test section. Hydrodynamic measurements were recorded at 100 Hz. USWGs and ADVs were hanging from a bridge-like structure above the test section. By sliding the bridge and repeating the wave run, data was recorded at twice the number of locations. This also allowed us to have repeated measurements from the in-line load cells with the same wave condition, which was useful to check the repeatability of the experiment. Details about the instrumentation placement is presented in Figure 6.

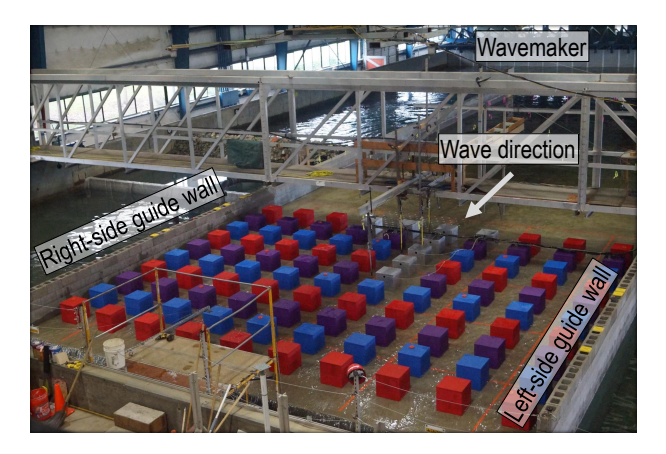


Figure 4: Overview of the OSU laboratory setup with the presence of the 10 x 10 building array.



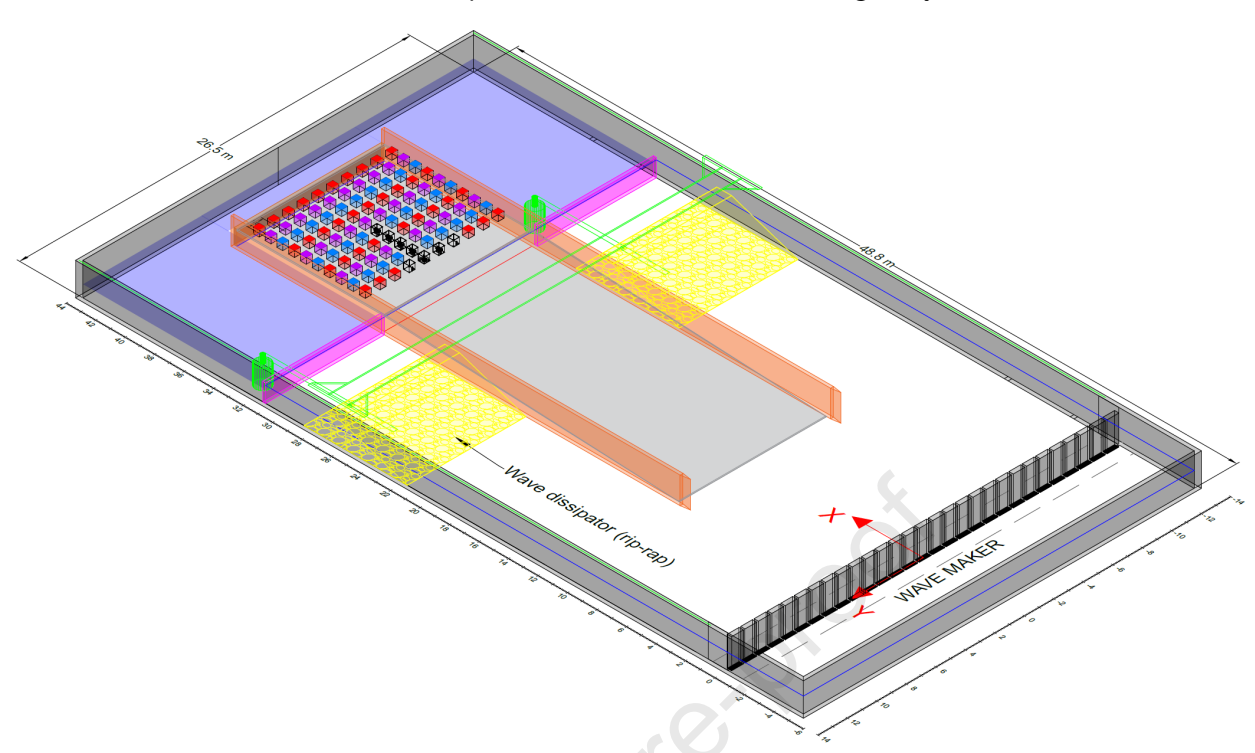


Figure 5: Graphic representation of the OSU laboratory setup.

3.2.2. Numerical setup

The resolution required to get a good agreement with the experimental data made infeasible the use of the full physical domain for our computing resources, therefore the width of the concrete beach was reduced from 10 m to 3 m (Figure 6b). After this reduction, three buildings per row were kept with one centered building per row from which numerical data was analyzed. The bottom profile and the structures were modelled using wall functions and a no-slip boundary condition whereas the sides of the 3 m width numerical domain a slip boundary condition was considered. The tsunami-like waves were generated using the piston-type wave boundary in olaFlow. Similarly to the validation against the HyTOFU experiment, an unstructured mesh was used, but with 5 different resolution regions (Figure A2). The grid resolution was increased from a coarse mesh until grid convergence was achieved, resulting in three final meshes (coarse, mid, and fine). More information about the different OSU meshes can be found in Appendix A.

3.2.3. Model performance

Due to the large number of wave gauges, the comparison between the experimental data and the model results are discussed for a few representative locations shown in Figure 7. A more complete comparison including all the wave gauges and all the ADVs is found in Appendix A. The free surface elevation in the sloping section is well represented by the model. The second wave that appears in the experimental data in WG2 is a wave reflected back from the wave dissipators (Figure 5) to the wavemaker and then to the concrete beach. This second wave does not appear in the simulations results because the numerical domain only includes a 3 m wide domain. Above the test section the model using the coarse mesh was not able to capture the rise of water in front of the

building located in the second row (USWG4), but using the mid and fine mesh good agreement is achieved. The agreement of the cross-shore velocity component from the model with the available data recorded by the ADV is reasonable. The gaps in the experimental data recorded from the ADVs exist because the device could not record the water velocity when a very foamy wave was passing through the instrument.

A visual comparison in Figure 8 presents a series of snapshots obtained both in the experiments and in the model ranging from when the $S_f=2.5\,\mathrm{s}$ wave is about to reach row 1 ($t=14.25\,\mathrm{s}$) to when the wave exerts the maximum load on row 1 ($t=15.25\,\mathrm{s}$). This comparison shows that in general the flow field is reasonably represented. The flow going through the cross shore streets is well captured by the simulation. Also, the water rising up in front of the structures located in row 1 is well captured by the model, showing good agreement regarding the amount of water piling up as a result of the blockage effect due to the presence of the structures.

Wave loading in the cross-shore direction (F) on the five specimens instrumented with inline load cells was reasonably captured by the model (Figure 9). There are two experimental wave loading time series because each experiment was repeated. The three meshes agree similarly to the data, except in areas where very complex water motion takes place. The simulated and recorded peak loads on row 1 for both trials have a difference up to a 24% and 19% for the coarse mesh, which is lowered to 15% and 11% for the fine mesh (Figure 10 and Table 1). A similar improvement in the agreement can be seen for the peak loads in row 2 for trial 2 as the resolution is increased. In rows 3, 4, and 5 the peak loads difference between the three meshes is considerably lower than for row 1 and 2. The largest relative errors of maximum loads was found in row 4, but surprisingly the smallest relative errors with the experimental data were found in row 5.

Table 1Maximum wave loading absolute and relative difference between the simulations and the experimental data. The comparison considers the structures located in rows 1 to 5.

		Absolute difference (N)				Relative difference					
Trial	Mesh	Row 1	Row 2	Row 3	Row 4	Row 5	Row 1	Row 2	Row 3	Row 4	Row 5
1	Coarse Mid Fine	34.0 29.3 21.8	-12.1 -6.1 17.6	-14.3 -14.8 -13.7	-15.9 -8.7 -12.4	0.7 3.1 1.7	20.7%	-11.0%	-30.7%	-42.1% -22.9% -32.8%	20.0%
2	Coarse Mid Fine	28.3 23.5 16.0	-25.4 -19.4 4.3	-14.0 -14.5 -13.4	-10.5 -3.3 -7.0	-0.1 2.4 1.0	19.2% 16.0% 10.9%	-28.2%	-29.2% -30.3% -27.9%		-0.4% 14.5% 6.0%

4. Methodology

When designing tsunami resistant residential buildings, large scale numerical models can be used to estimate the flow properties at the building location, which may explicitly consider large infrastructure, such as breakwaters, ports, and seawalls. However, the inclusion of small scale structures with sizes comparable to the grid resolution (like houses, hotels, restaurants) is not always possible due to computer power limitations. Traditionally, small scale structures are not explicitly

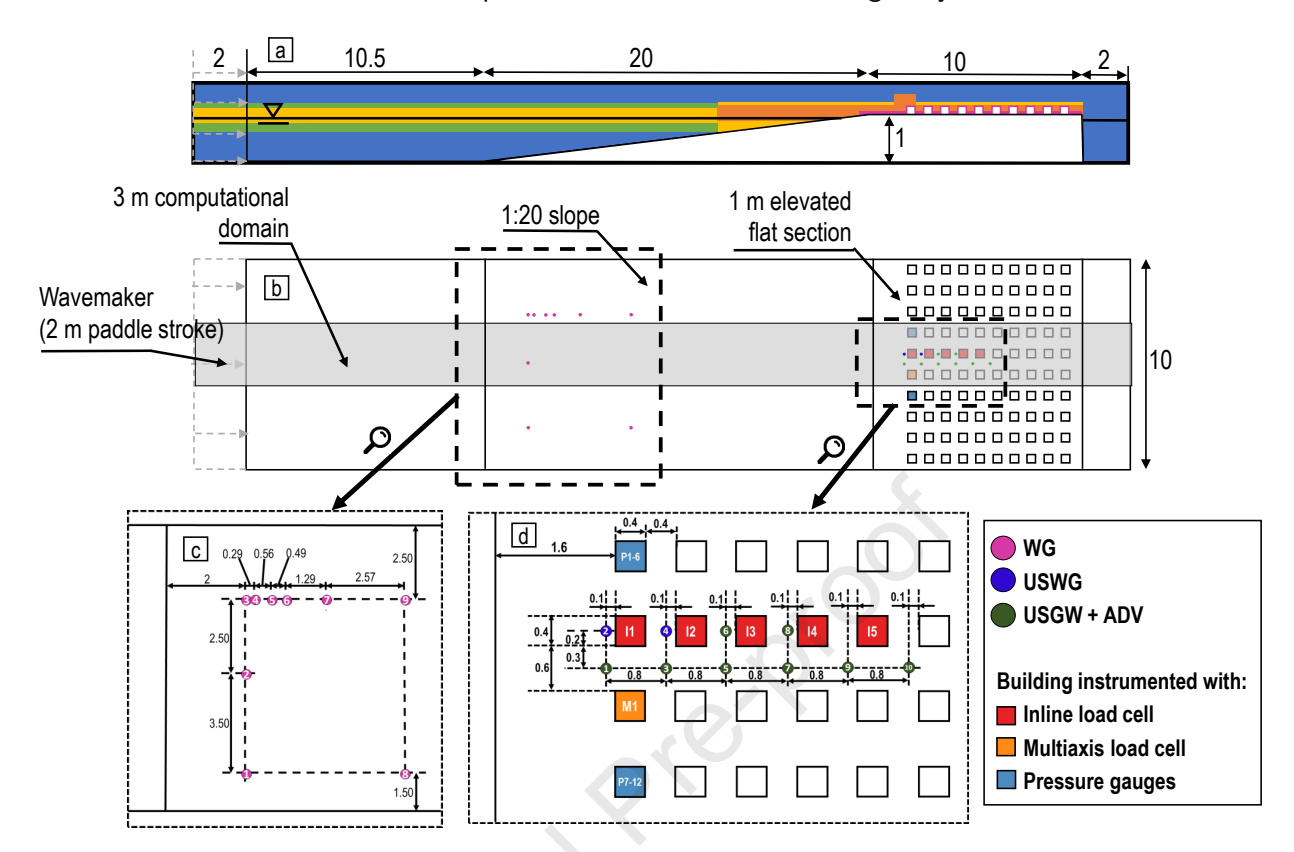


Figure 6: Plan and side elevation view of the OSU Experimental set up including the location of resistance wave gauges, ultrasonic wave gauges, ADVs, and instrumented buildings.

included in the models, resulting in computations over open ground sometimes called bare earth simulations. Although small scale buildings have been included in depth averaged models by using a friction coefficient, it may not be an appropriate approach if the goal is to predict shielding in a building array. The following methodology aims to predict how wave loading in buildings is affected by the presence of a building array.

4.1. Simulations with the building array

As presented in section 3.2, experimental maximum loads decrease as the number of rows of buildings providing shelter increases (Figure 10). Our study focuses on how the number of rows providing shelter influences the wave load on a building of interest. This is obtained by comparing the wave load in the shielded building and the wave load on the same building when it is unobstructed (i.e. with no buildings in front of it). The OSU experiment setup was selected as our base case, using the reduced section width of 3 m presented in the validation. This reduction significantly decreased the required computing power. The computational domain considers 3 buildings per each row, with a total of 10 rows. As our validation showed, the fine mesh led to the best agreement with the experimental data presented in the section 3.2. This mesh was used in all the simulations.

A set of 10 simulations for each wave condition was conducted by sequentially removing the frontmost row of buildings remaining, starting from the base case. The base case contains all 10

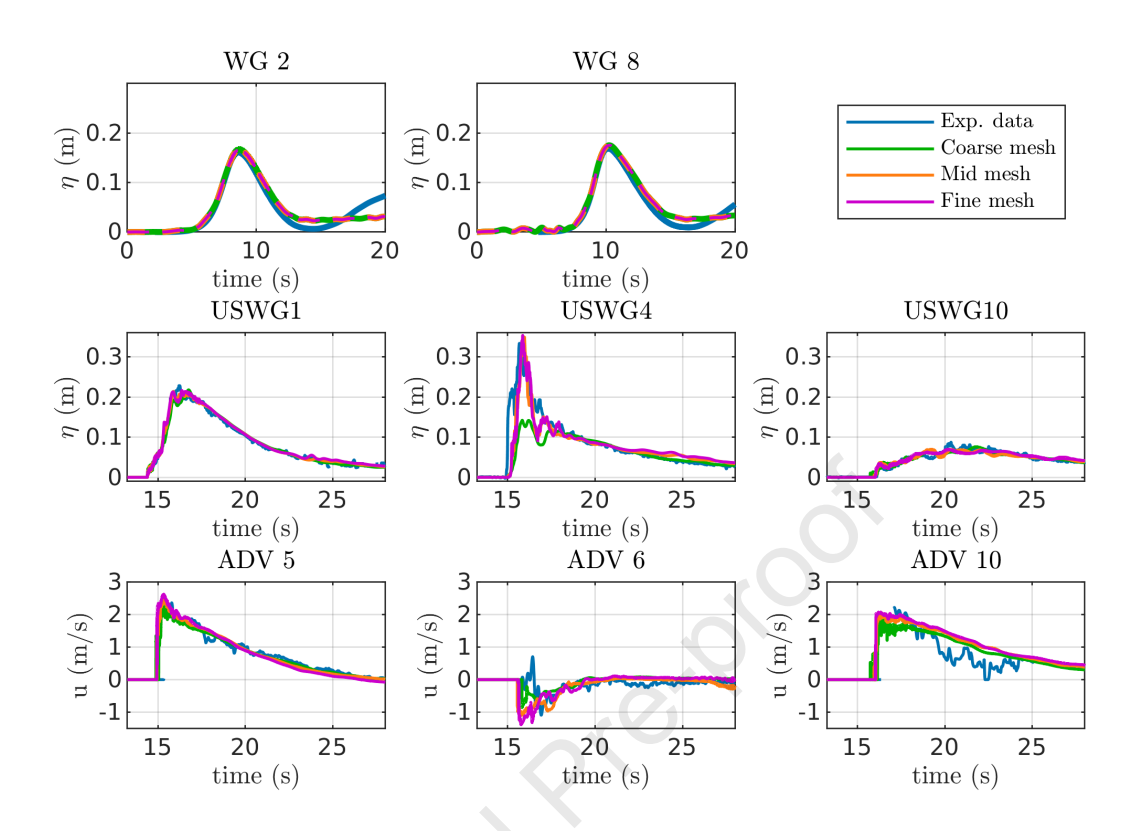


Figure 7: Free surface elevation and horizontal velocity component comparison between the experimental data and the three different meshes used.

rows, with row 1 being the unobstructed row. By removing the frontmost row of buildings from the base case, a simulation with rows 2 through 10 is obtained, from which we get the unobstructed loads on row 2. After sequentially repeating this process for subsequent rows, a set of 10 simulations per wave condition is obtained, where each simulation yields unobstructed wave loading for each row. A breaking wave ($S_f = 2.5$ s) and a non-breaking wave ($S_f = 4.0$ s) were generated by a piston-type boundary condition moving through a distance of 2 m on the left side of the flume. The displacement over time of the piston during the wave generation is given by Equation (8).

4.2. Bare Earth simulations

As previously mentioned, when modeling tsunami flows over large areas in developed regions, due to current computational limitations, buildings are generally eliminated when they are smaller than the grid spatial resolution of large scale wave models. In this paper we refer to simulations without buildings as bare earth simulations. Bare earth simulations are useful because, with the buildings being removed from the domain, we get undisturbed flow conditions that enable us to compare the bare earth hydrodynamics with the non bare earth wave loads. A bare earth simulation was conducted for each wave condition.

Among the different hydrodynamic properties that can be obtained from bare earth simulations, the instantaneous momentum flux has been used in the past to predict wave loading (Yeh, 2006). In practice, design standards use values proportional to the momentum flux to estimate wave loading

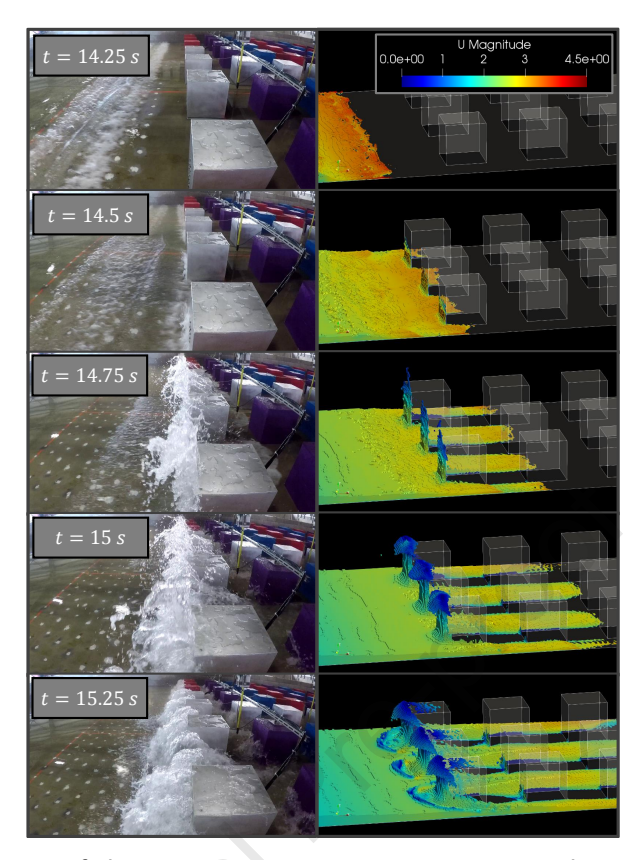


Figure 8: Visual comparison of the $S_f=2.5$ s wave impact on row 1 between the recording from an action camera placed above the test section and the numerical results. The timestep between snapshots is $\Delta t=0.25$ s, ranging from t=14.25 s to t=15.25 s. The numerical results were obtained using the fine mesh.

in vertical structures (ASCE7-16, 2017; FEMA, 2012). The instantaneous horizontal momentum flux (M) is defined as

$$M = b \int_0^{\eta} \left(p + \rho u^2 \right) dz \tag{9}$$

where p is the instantaneous pressure, ρ is the water density, η is the instantaneous free surface elevation, u is the instantaneous horizontal water velocity, and b is the alongshore width where the momentum flux is calculated. The momentum flux is compared to wave loads on the buildings, therefore b = 0.4 m is used to calculate momentum fluxes.

4.3. Dimensionless parameters

To keep the analysis as general as possible, this study works with dimensionless parameters. The bare earth momentum flux is normalized as

$$M^* = \frac{M}{b\rho g \{ \eta(t_{M-1}) \}^2} \tag{10}$$

where M^* is the dimensionless momentum flux, $t_{M_{\rm max}}$ is the time when the momentum flux is maximum, and b=0.4 is building width. Wave loading on the structures is normalized by Eq. 11

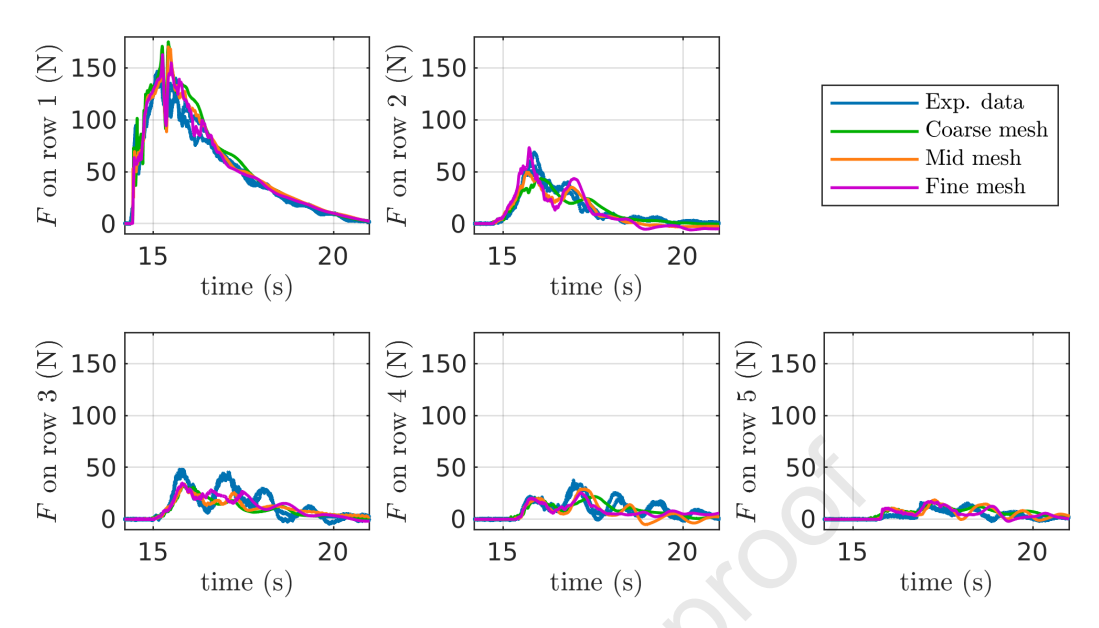


Figure 9: Comparison between the experimental wave loading on the first five rows and the wave loading obtained from the simulations using the coarse, mid, and fine meshes.

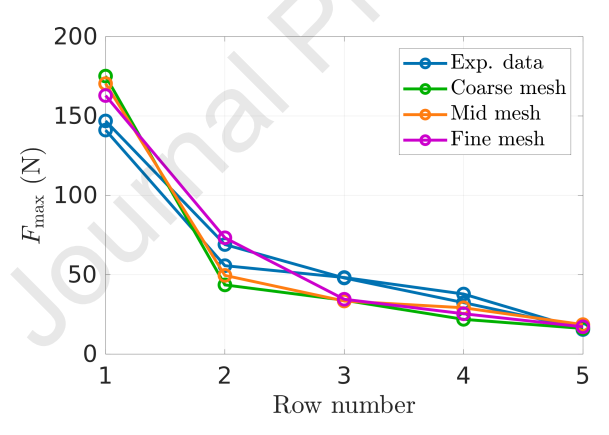


Figure 10: Maximum wave loading comparison between the experimental data and simulations using the coarse, mid, and fine meshes.

$$F^* = \frac{F}{b\rho g \{ \eta(t_{M_{\text{max}}}) \}^2}$$
 (11)

where F^* is the corresponding instantaneous dimensionless horizontal load, and F is the instantaneous horizontal component of the force in the structure, which is obtained by subtracting the load on the back face of the structure to the load of the front face of the structure. To obtain this dimensionless load, it is necessary to use values from two different simulations: the simulation including the building (this gives the load F) and a bare earth simulation (this gives $\eta(t=t_{M_{\max}})$). Time is normalized following the Eq. (12)

$$t^* = (t - t_{\text{row 1}}) \sqrt{\frac{g}{\eta(t_{M_{\text{max}}}, x_{\text{row 1}})}}$$
 (12)

where $\eta(t_{M_{\max}}, x_{\text{row 1}})$ is a representative bare earth free surface elevation, defined as η when $t = t_{M_{\max}}$ at the location $x_{\text{row 1}}$, which corresponds to the bare earth position where the front face of the structure in row 1 would be located. $t_{\text{row 1}}$ is the time when the water reaches $x_{\text{row 1}}$.

5. Results

We define $F_n^{(l)}$ as the normalized, cross-shore direction, wave loading on the building located in row l with n number of rows in front of the building providing shelter, and $M_{BE}^{(l)}$ as the normalized, cross-shore direction, bare earth momentum flux in the at the location of the row l. The superscript * is removed to simplify our notation.

5.1. Wave load reduction as a function of the number of rows providing shelter

To evaluate the wave load change depending on the presence of the building array, we introduce three simple metrics: Load Reduction Factors A, B, and C, which are defined in equations (13), (14), and (15) respectively.

$$LRFA_n^{(l)} = \frac{F_{n,\text{max}}^{(l)}}{F_{0,\text{max}}^{(l)}}$$
(13)

$$LRFB_n^{(l)} = \frac{F_{n,\text{max}}^{(l)}}{F_{0,\text{max}}^{(l-n)}}$$
 (14)

$$LRFB_{n}^{(l)} = \frac{F_{n,\text{max}}^{(l)}}{F_{0,\text{max}}^{(l-n)}}$$

$$LRFC_{n}^{(l)} = \frac{F_{n,\text{max}}^{(l)}}{M_{BE,\text{max}}^{(l)}}$$
(14)

LRFA_n^(l) measures the ratio between the maximum wave loading on the structure located in the row l when n number of rows of structures provide shelter ($F_{n,\max}^{(l)}$) to the maximum unobstructed wave loading on the same structure $(F_{0,\max}^{(l)})$. LRFA_n gives the direct change in maximum wave loading for a structure located in row l. Note that to obtain the ratio LRFA_n^(l) for a given row l, two simulations are required: one with the unobstructed structure and one with a building array in the

 $LRFB_n^{(l)}$ measures the ratio between the maximum wave loading on the structure located in the row *l* when *n* number of rows of structures provide shelter $(F_{n,\max}^{(l)})$ to the maximum unobstructed wave loading on the frontmost structure $(F_{0,\max}^{(l-n)})$, located in the row l-n. Although LRFB_n^(l) does not give a direct measurement of the maximum load change on row l, it offers the benefit that its calculation only require the results from one laboratory experiment or one computational run. This is particularly useful when dealing with data from laboratory experiments, since modifying the setup is not as straightforward as it is for numerical experiments.

 $LRFC_n^{(l)}$ measures the ratio between the maximum wave loading on the structure located in the row l when n number of rows of structures provide shelter $(F_{n,\max}^{(l)})$ to the maximum bare earth

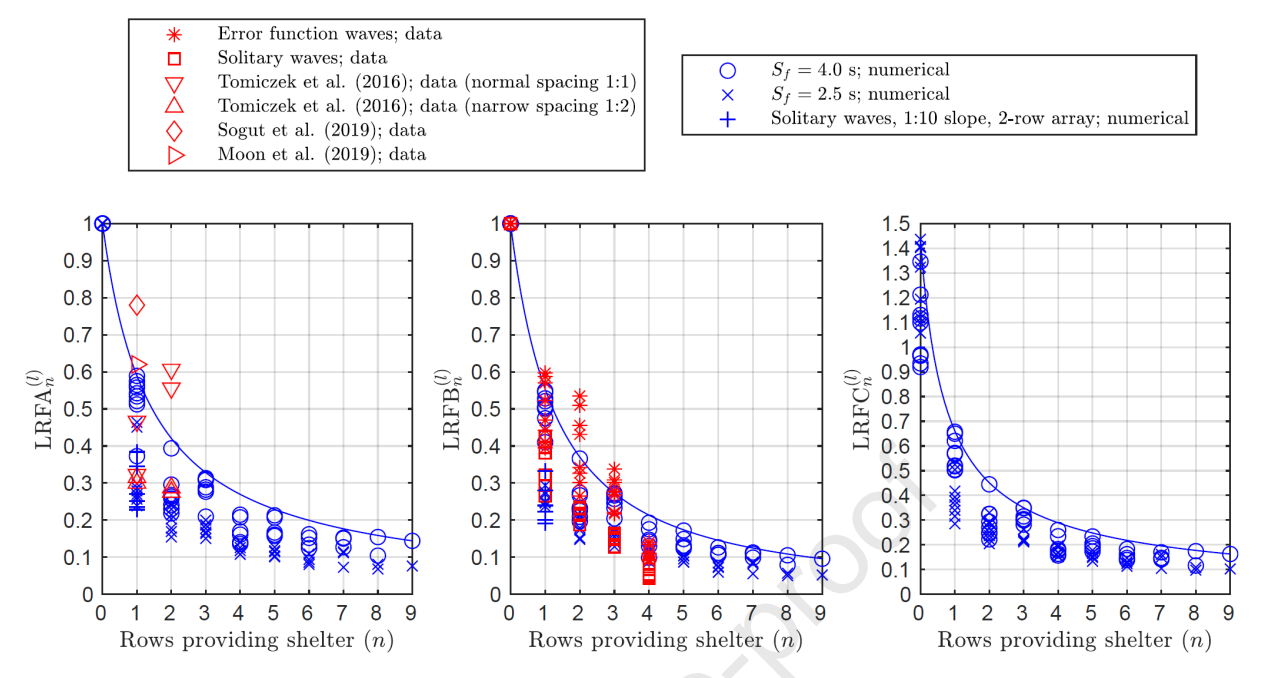


Figure 11: Load Reduction Factors LRFA_n^(l), LRFB_n^(l), and LRFC_n^(l) as a function of the number of rows providing shelter (n) with their respective envelopes.

momentum flux $(M_{BE,\max}^{(l)})$ at the location of row l. We introduce $LRFC_n^{(l)}$ because the calculation of the load reduction factors $LRFA_n^{(l)}$ and $LRFB_n^{(l)}$ needs an estimate for an unobstructed load. To estimate wave loading on a structure it is necessary to place the actual structure in the numerical domain and to vertically solve the flow hydrodynamics requiring a large amount of computing power. However, bare earth momentum fluxes are possible to obtain from simpler depth averaged models which do not necessarily require neither the actual placing of the structure nor a high resolution mesh around the structure location. Therefore, $LRFC_n^{(l)}$ is a useful load reduction factor because it could be simply multiplied by $M_{BE,\max}^{(l)}$ to give an estimate for the sheltered maximum wave loading.

Combining the set of 10 simulations along with the bare earth case, per each wave condition, Load Reduction Factors A, B, and C were obtained for structures on all the l-rows (Figure 11). Upper envelopes for LRFs values are presented in equations (16), (17), and (18)

$$LRFA_{env} = \frac{1}{(1 + 0.748 \cdot n)^{0.947}}$$
 (16)

LRFB_{env} =
$$\frac{1}{(1 + 0.596 \cdot n)^{1.267}}$$
 (17)

$$LRFC_{env} = \frac{1.437}{(1 + 1.719 \cdot n)^{0.777}}$$
 (18)

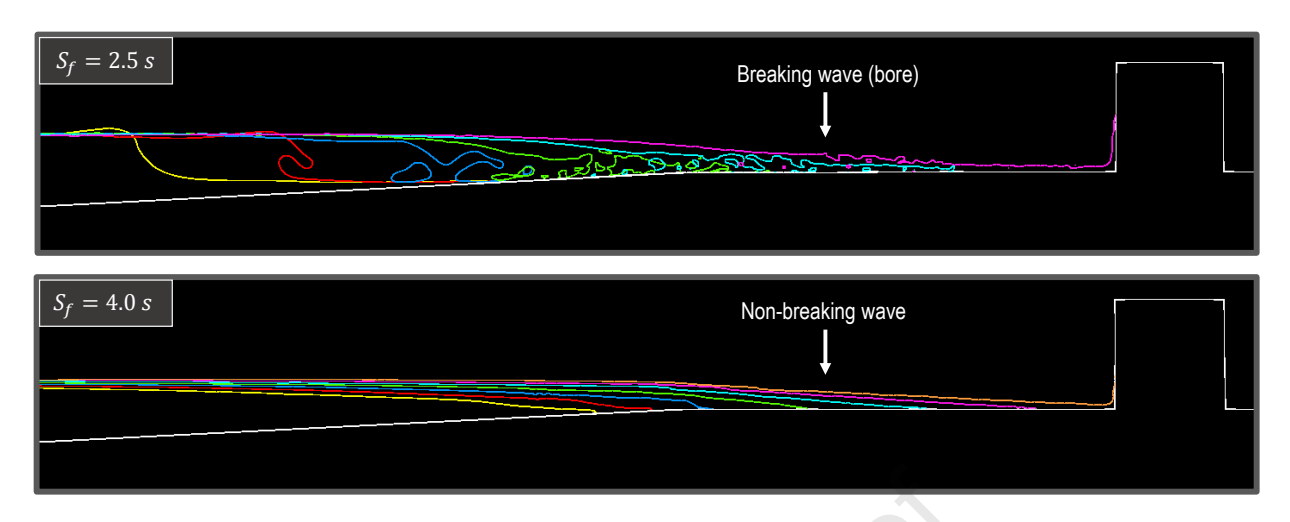


Figure 12: Snapshots separated by 0.25 s intervals of the $S_f = 2.5$ s breaking wave condition and the $S_f = 4.0$ s non-breaking wave condition.

6. Discussion

In general, LRFA values monotonically decrease as more n rows provide shelter (Figure 11). $F_{n,\max}^{(l)}$ not only decreases as n increases, but also the rate of sheltering decreases as n increases, which is measured by the slope of the LRF upper envelopes. The greatest load reduction rate was found when going from n=0 rows to n=1 row providing shelter, with maximum LRFA values going from LRFA $_{n=0}^{(l)}=1$ to LRFA $_{n=1}^{(l)}=0.59$. When sheltering is provided by 4 or more rows, maximum LRFA values are below 0.22, meaning that maximum loads can be up to about 4 times less than the corresponding unobstructed load if more than 4 rows are providing shelter. After n=4, there is not a significant decrease in maximum loads, meaning that most of the load reduction takes place in the first 4 rows of structures.

Although both wave conditions were generated using a 2 m stroke error displacement function for the wave paddle, the $S_f=2.5$ s wave had a faster paddle speed than the $S_f=4.0$ s wave, resulting in a more energetic breaking wave and therefore a greater wave height was obtained. The $S_f=2.5$ s wave broke right before the end of the slope generating a turbulent bore that impacted the structures whereas the less energetic $S_f=4.0$ s wave did not break, resulting in a non-breaking wave that collided the structures (Figure 12). This difference seems to be important when quantifying the sheltering effect, shown by a tendency for the three LRFs to increase with increasing S_f (Figure 11). Similar findings have been found for maximum pressure reduction on structures inside a 3 x 3 building array, where the reduction was more noticeable for wave breaking conditions (Figure 13 in Tomiczek et al., 2016). This effect was also found for maximum loading reduction on shielded elevated structures, with a significantly less load reduction for non-breaking wave conditions (Figure 12 in Winter et al., 2020).

LRFC tends to be larger than 1 for no rows (n = 0) providing shelter (Figure 11). This shows that for our particular setup the maximum loads are greater than the maximum bare earth momentum flux when no shelter is provided. Wave loading greater than momentum flux has been found in other studies involving wave loading on single structures. Linton et al. (2013) found that maximum

values of transient loads were within 20% of values derived from the linear momentum equation and Robertson et al. (2013) found through laboratory experiments of solitary waves impact on structures over a wet bed that maximum experimental loads are larger than momentum flux based design formulae.

A closer look to the time series of $F_0^{(1)}$ and $M_{BE}^{(1)}$ shows that the underestimation of the maximum wave loading is likely to occur at the peak location (Figure 13). There is a very strong agreement between both quantities away from the peak location when $M_{BE}^{(1)}$ is compared to the load without subtracting the back face load. However, at the peak location, there is no significant difference between the load only in the front face and the load considering both the front and the back faces. A comparison between maximum unobstructed loads and maximum bare earth momentum fluxes in the location of all 10 rows shows that the difference between them increases for the $S_f = 2.5$ s breaking condition, which is presented in the two clusters of data points differentiated by the wave condition (Figure 14). We believe this happens because the splash-up after the impact increases water levels for a short amount of time and therefore increases the total wave loading (Figure 13), a situation that does not happen with the bare earth condition.

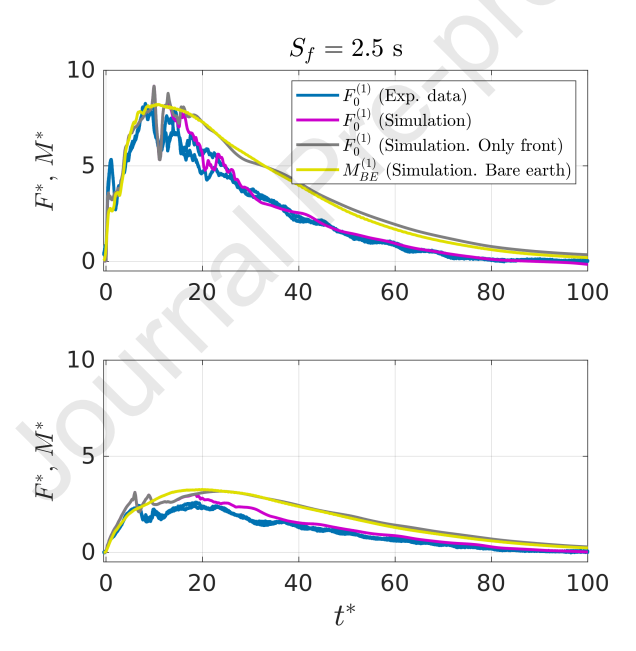


Figure 13: Comparison between the instantaneous dimensionless bare earth momentum flux $(M_{BE}^{(1)})$ at the location of the front face of the building in row 1, the unobstructed dimensionless load $(F_0^{(1)})$ on the building located in row 1, and the dimensionless load only on the flow facing face of the building, and experimental data, for both $S_f = 2.5$ s and $S_f = 4.0$ s wave conditions.

When there is at least 1 row providing shelter LRFC values are less than 1, with maximum wave loads being overestimated by the maximum bare earth momentum flux, and similarly to LRFA, both the sheltering effect and the rate of sheltering decreases as *n* increases, with most of the reduction occurring in the first 4 rows.

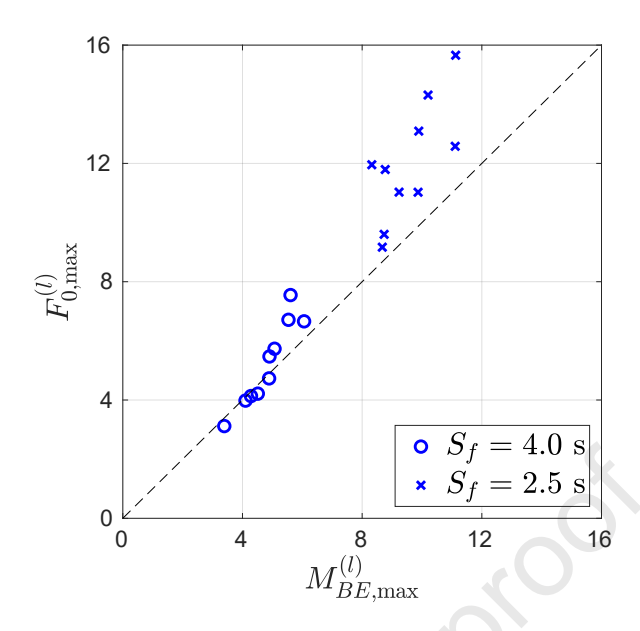


Figure 14: Comparison between the maximum instantaneous bare earth dimensionless momentum flux $(M_{BE,\max}^{(l)})$ at the location of the unobstructed building l and the maximum unobstructed dimensionless load $(F_{0,\max}^{(l)})$ at the row l.

6.1. Comparison with additional wave conditions

As a part of this study, in addition to the $S_f=2.5\,\mathrm{s}$ and $S_f=4.0\,\mathrm{s}$ scale factors waves, we tested in the laboratory wave conditions with scale factors of $S_f=2.0\,\mathrm{s}$ and $S_f=3.0\,\mathrm{s}$, and solitary waves with wave heights of $H=0.075\,\mathrm{m}$, $H=0.15\,\mathrm{m}$, and $H=0.20\,\mathrm{m}$. The difficulties inherent in large scale laboratory experiments did not allow us to modify the setup, which was fixed to the $10\,\mathrm{x}$ 10 array of structures. Therefore, experimental values of LRFA were not possible to obtain; however ratios of LRFB could be obtained, because this reduction factor is normalized by the maximum load in the frontmost row. Reduction factors from these additional experimental wave conditions, which are within the range of simulated values of LRFB (Figure 11).

Additional numerical simulations were conducted in this study with the same features as the base case, but with a reduced 2-row building array. A steeper beach slope of 1:10 was used. The initial water level was 0.75 m, and the elevation of the test bed was 0.795 m. Solitary waves of H = 0.1 m, H = 0.175 m, H = 0.25 m, H = 0.325 m, H = 0.40 m, and H = 0.475 m were generated by specifying the solitary boundary condition in olaFlow, which generates a solitary wave at the location of the wavemaker according to the Boussinesq theory as described in Higuera et al. (2013). These conditions allowed us to have a wider range of wave conditions that complements the main 10-row building array simulations. The reduction factors from these additional numerical tests are within the rest of the simulated values (Figure 11)

6.2. Comparison with other studies

Tomiczek et al. (2016) conducted laboratory experiments where instantaneous pressure was recorded in the on buildings located within a 3 x 3 array. The bathymetry and wave conditions are the ones used in the validation presented in section 3.1. The maximum pressure recorded in

Table 2 Protection factor (*Prot br*) as a function of the row location in the PTVA-3 Model.

Row location	1	2 to 3	4 to 6	7 to 10	>10
Prot_br	0	+0.25	+0.5	+0.75	+1

the front face of the specimen was compared to the unobstructed condition. By moving the instrumented specimen and repeating the experiments, the change in maximum pressure was measured for both the second row and the third row. This was done for a spacing ratio between building spacing to building width of 1:1 and then for a narrower ratio of 1:2. The reduction in maximum pressure is presented in Figure 11 along with LRFA values. Most of the data values from Tomiczek et al. (2016) pressure reduction values lie below the equation (16) envelope, except from the pressure reduction values in the third row, with 1:1 spacing. Moon et al. (2019) performed a set of experiments where pressure was recorded in the front face of a specimen within a 2-row building array with different configurations and different wave conditions. The closest array configuration to the setup in this paper is defined in Moon et al. (2019) as the non-overtopping wave condition 3F case, which is a 3 x 2 building array. Under this configuration, the seaward face experienced a maximum pressure reduction of 38%, which if translated to a corresponding LRFA-like value it would be equal to 1 - 0.38 = 0.62, with 1 row providing shelter. This value lies above the upper envelope by a small difference of 0.04. However, a point to consider is that data from Tomiczek et al. (2016) and Moon et al. (2019) correspond to maximum pressures which, as found in the study of splash-up of tsunami bore impact by Ko and Yeh (2018), does not necessarily happen at the same time as maximum wave loading values. Sogut et al. (2019) studied the pressure change on a building located in the second row of a 2-row, 3 x 2 building array, with the same relative spacing found in Moon et al. (2019). It was found that when the first row is present, the maximum pressure is reduced by 22% compared to the unobstructed case maximum pressure. The equivalent LRFA value would be equal to 1 - 0.22 = 0.78, which is located above the envelope. We believe that the main reason why this reduction factor is higher than the rest of the data points in Figure 11 is the fact that the bed was wet, allowing the wave to break right in front of the instrumented specimen. As noted by Oumeraci et al. (1993), when breaking occurs at a close distance from the specimen, the impact wave loading component may have a greater importance, potentially requiring a separate analysis.

6.3. Sheltering effect in the field and its applicability in vulnerability models

The decrease in wave loading as more rows of structures are providing sheltering has been observed indirectly by post-damage assessment (Reese et al., 2011; Fraser et al., 2013; Hatzikyriakou et al., 2016; Tomiczek et al., 2017). The PTVA-3 vulnerability model (Dall'Osso et al., 2009) uses a building row protection factor ($Prot_br$) as one of its independent variables that goes from 0 (very low protection) to 1 (very high protection), depending on the row location measured from the closest building to the shoreline (Table 2). Although $Prot_br$ values were obtained from post-damage surveys, when transformed to a reduction-like factor $(1 - Prot_br)$, the resulting step function has similar magnitudes to the presented LRF values, which could potentially indicate that the reduction on maximum wave loading might be related to post-tsunami observed sheltering effects.

6.4. Blocking ratio, cross-shore spacing, and offset effects

One of the biggest limitations of this study is the fixed laboratory geometry from which the results were obtained. As studied before by Yang et al. (2018), the width and distance of the buildings providing shelter significantly influence the sheltering effect. However, analysis of all possible combinations is infeasible with our current computer resources. Given these limitations, we studied the sensitivity of the load reduction by changing: (1) the blocking given by the buildings in row 1 to the buildings in row 2 by changing the width of the buildings in row 1, (2) the clear distance between the building in row 1 to the building on row 2, and (3) a lateral offset distance between row 1 and row 2.

We define a relative blocking ratio (w^*) as $w^* = w/c$, where w and c are the width and the maximum possible width of the buildings in row 1, respectively (Figure 15). Note that w^* varies from $w^* = 0$ (no sheltering) to $w^* = 1$ (full sheltering). The relative distance between the building in row 1 to the building on row 2 (d^*) is defined as $d^* = d/b$, where d and b = 0.4 m are the cross shore distance between the first two rows and the width of the building in the second row, respectively. Magnitudes vary from $d^* = 0$ (no distance between row 1 and row 2) to $d^* \to \infty$ (no sheltering). The relative offset between buildings in row 1 and buildings in row 2 (o^*) is defined as $o^* = o/(0.5c)$, where o and 0.5c = 0.5 m are the offset and the maximum possible offset between between the first two rows, respectively. o^* varies from $o^* = 0$ (no offset) to $o^* = 1$ (row 2 fully exposed to the flow)

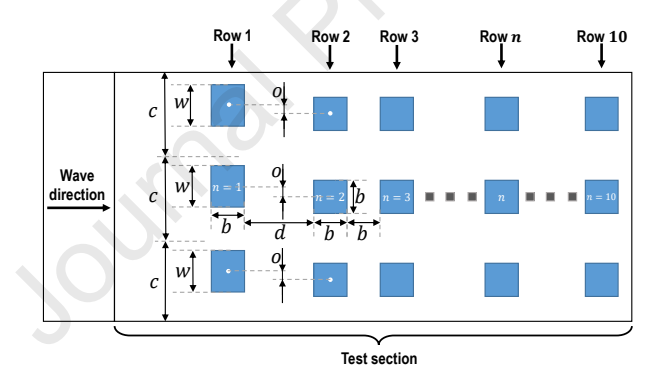


Figure 15: Detail of the distances used to compute the relative blocking ratio w^* , relative distance d^* , and relative offset o^*

6.4.1. Building width effects

The effect of the width w^* on the maximum load in the structure located in row 2 was analyzed keeping the relative distance $d^*=1$ constant and with no offset $(o^*=0)$. The normalized maximum load in row 2 normalized by its unobstructed maximum load (LRFA $_{n=1}^{(l=2)}$) is shown in Figure 16. It can be seen that when $w^*>0.4$ there is a clear monotonic reduction in LRFA $_{n=1}^{(l=2)}$ as w^* increases, for both $S_f=4.0$ s and $S_f=2.5$ s wave conditions. Similar findings are reported in Yang et al. (2018). However, when there is a smaller obstacle providing sheltering ($w^*<0.4$) the reduction in the maximum load LRFA $_{n=1}^{(l=2)}$ does not decrease monotonically. The explanation for this is not clear and it is subject to further analysis.

6.4.2. Cross-shore spacing effects

The effect of the distance d^* on the maximum load in row 2 normalized by its unobstructed maximum load (LRFA $_{n=1}^{(l=2)}$) was analyzed by keeping the relative width $w^*=0.4$ constant and $o^*=0$ with no offset (Figure 16). For the $S_f=2.5$ s breaking wave condition there is a monotonic increase in LRFA $_{n=1}^{(l=2)}$ as the obstacle is located further away. For the $S_f=4.0$ s non breaking wave condition there is a monotonic increase in LRFA $_{n=1}^{(l=2)}$ when $d^*<2.5$ as the obstacle is located further away. For values of $2.5 < d^* < 4$ there is a slight decrease in LRFA $_{n=1}^{(l=2)}$ as the obstacle is located further away. This could suggest that for non-breaking surges there is only a range of d^* values where the sheltering effect does not increase when d^* decreases. Similar results have been found in Tomiczek et al. (2016), who experimentally showed that the reduction in peak pressures in sheltered structures is increased when reducing the spacing between them (Figure 11). Yang et al. (2018) found through numerical experiments that a force mitigation effect is significantly reduced when the distance between structures is larger than a certain threshold.

6.4.3. Offset effects

The effect of the offset o^* on LRFA $_{n=1}^{(l=2)}$ is presented in Figure 16. The relative width w^* and the relative distance d^* were kept constant with values of 0.4 and 1, respectively. In general, for all the values of o^* , there is a larger reduction of the maximum load for the broken $S_f = 2.5$ s wave case than for the unbroken $S_f = 4.0$ s wave case. The offset has a strong effect in the maximum load mitigation. When no offset is considered ($o^* = 0$), the load reduction was found to be approximately 0.5, whereas when a full offset is present ($o^* = 1$) practically no load reduction exists. There is even a slight increase on the load by a factor of 1.04 for the unbroken $S_f = 4.0$ s wave case, meaning that the maximum wave loading could even be amplified by offset effects. We believe this load increase is due to the increase on the velocity as a result from the flow constriction between the obstacles on the first row. This was found by Nouri et al. (2010), where maximum loads were amplified by a factor up to 1.25 for the cases presenting a flow constriction. However, they considered an initially inundated bed, and, when translating experimental distances to our relative width and distance ratios, the relative width was found to be similar to 0.4, with a value of $w^* = 0.375$, but the relative cross-shore distance between the obstacles and the test structure was $d^* = 7.0$, a value much larger than the $d^* = 1.0$ used in our numerical tests. Thomas et al. (2015) studied the change of maximum run-up loads by testing experimentally different symmetric offset configurations by changing a wake clearance angle β , defined as the angle between the cross-shore line passing through the center of the instrumented specimen and the line passing from the front center of the instrumented specimen and the frontside inside edge of one of the buildings in the front. When $o^* = 1$, the wake clearance angle β could be related to the distances shown in Figure 15 by $\beta = \arctan\{[c-w]/[2(d+b)]\}$. Thomas et al. (2015) found that for small wake clearance angles (< 12°) the maximum force was reduced by about 40%. However, for wake clearance angles between 20° and 35° the maximum force was amplified by about 40% when compared to the unobstructed case. This suggests that for $o^* = 1$ and $\beta < 35^\circ$, depending on the ratio of the channel width (c - w) to the cross shore distance (d + b), the maximum loads could be mitigated or increased in the second row. Winter et al. (2020) conducted laboratory experiments on tsunami loading over elevated structures. Similarly to our experiments, a broken and an unbroken wave were considered. Several offset configurations were tested, but here we refer to the case E on Winter et al. (2020), which after translating their geometry to our dimensionless distances, it would have

a relative offset of $o^* = 1$, relative width of $w^* = 0.45$, and a relative distance of $d^* = 1.39$. Under these conditions, the maximum load for the broken wave case was increased by roughly 10%, while for the unbroken case the maximum load was reduced by 10%.

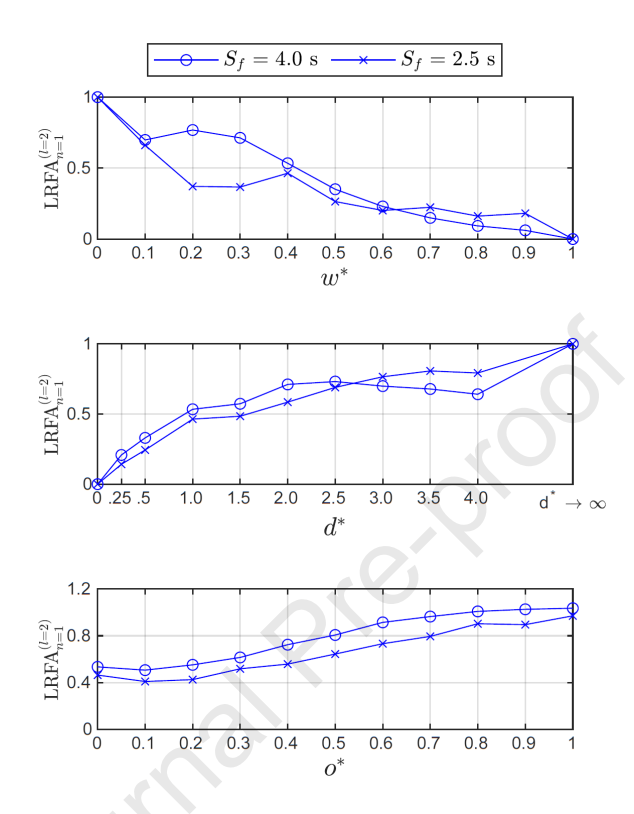


Figure 16: LRFA $_{n=1}^{(l=2)}$ as function of the relative blocking ratio w^* , the relative distance d^* and the relative offset o^* . Values of $w^* = 0.4$, $d^* = 1.0$, and $o^* = 0$ were kept unless the horizontal label states otherwise.

6.5. Effect of the building array on maximum inundation levels, cross-shore velocity, and cross-shore momentum flux

As discussed in previous sections, wave loading is reduced as more rows of buildings provide shelter, which means that the energy from the wave collision that an unobstructed building would receive is reflected back offshore, dissipated in the building array, deflected through the cross-shore streets, or a combination of the above. In this subsection we investigate the change in maximum inundation levels, cross-shore velocity, and cross-shore momentum flux in the cross-shore streets of the building array.

We define $\eta_{n,\max}^{(l)}$ as the maximum free surface elevation at the row l with n rows in the front providing shelter. This quantity is evaluated between structures along the cross-shore centerline (i.e. the center street that is perpendicular to the shoreline). Similarly to the wave loading reduction factors, we define a run-up reduction factor RRF as follows in equation (19).

$$RRF = \frac{\eta_{n,\text{max}}^{(l)}}{\eta_{\text{BE, max}}^{(l)}}$$
 (19)

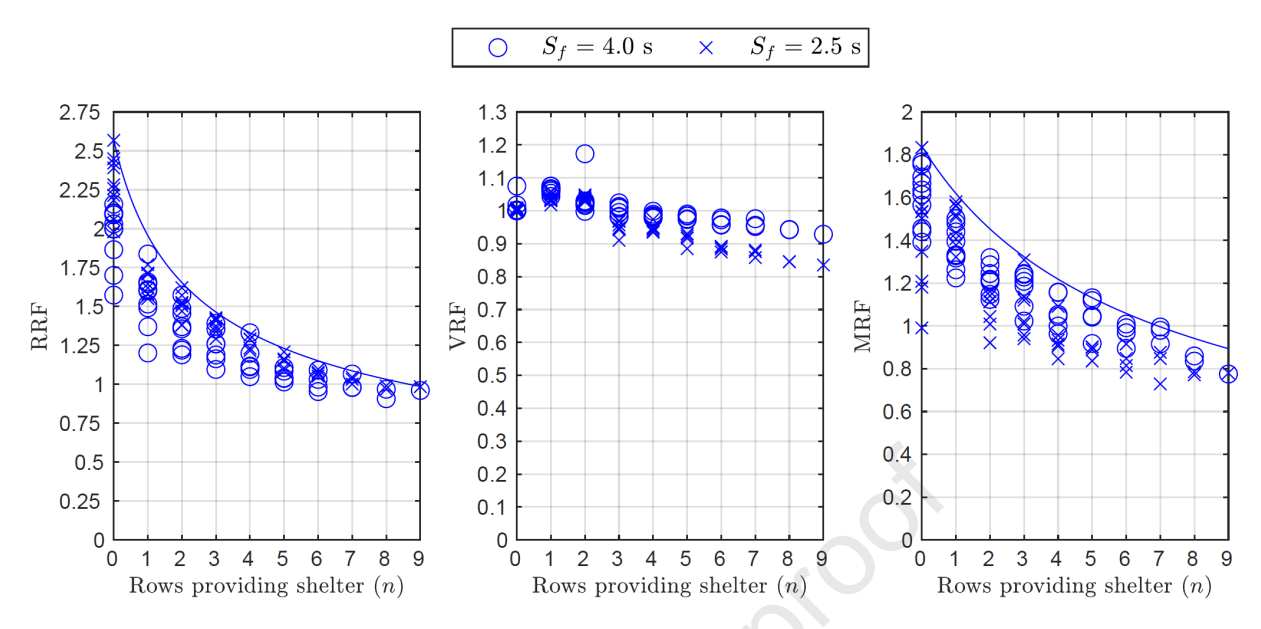


Figure 17: Numerical run-up reduction factors (RRF), velocity reduction factors (VRF), and momentum flux reduction factors (MRF) as a function of the number of rows providing shelter (n)

where $\eta_{\text{BE,max}}^{(l)}$ is the maximum bare earth free surface elevation. There is a considerable increase in maximum inundation levels in the cross-shore street $\eta_{n,\max}^{(l)}$ due to the presence of the building array (Figure 17). When bare earth inundation levels in the cross shore street between the beach's first row of buildings (n=0) are compared to bare earth levels, the increase in the maximum free surface elevation reached values up to 2.57 times higher than bare earth levels. One physical interpretation of the increase in maximum inundation levels is that the flow has to follow the continuity equation (Eq. 1) which may lead to an increase of the water levels due to a flow constriction once entering inside the building array. As more rows provide shelter, RRF values monotonically decrease. It seems that the presence of the building array has a negative impact on the inundation levels for the first rows. An increase in maximum inundation levels was also experimentally found by Ishiii et al. (2019), but only considering 1 row of buildings. There is a neutral effect when enough sheltering is provided, with RRF values close to 1 when $n \ge 8$. For this particular setup that we tested, lower maximum wave loading on shielded structures does not necessarily mean lower inundation levels. An upper envelope for RRF is presented in equation (20).

$$RRF_{env} = \frac{2.57}{(1 + 0.846 \cdot n)^{0.445}}$$
 (20)

The change in maximum cross-shore velocity in the cross-shore street is also briefly studied. A velocity reduction factor VRF is defined following the equation (21)

$$VRF = \frac{u_{n,\text{max}}^{(l)}}{u_{BE\text{ max}}^{(l)}}$$
 (21)

where $u_{n,\max}^{(l)}$ is the maximum horizontal velocity at the row l with n rows in the front providing shel-

ter and $u_{BE,\max}^{(l)}$ is the maximum horizontal velocity with bare earth conditions, with both quantities evaluated at the same location where RRF is evaluated. There is a slight increase in the horizontal velocity in the first rows due to the presence of the building array and a slight decrease of the horizontal velocity when $n \ge 4$ (Figure 17), but overall there is not a significant change from bare earth maximum horizontal velocities.

The change in maximum momentum flux in the cross-shore street when compared to bare earth conditions is shown in Figure 17, where MRF is the momentum flux reduction factor defined by equation (22)

$$MRF = \frac{M_{n,\text{max}}^{(l)}}{M_{BE,\text{max}}^{(l)}}$$
 (22)

where $M_{n,\max}^{(l)}$ is the maximum momentum flux at the row l with n rows in the front providing shelter. Both $M_{n,\max}^{(l)}$ and $M_{BE,\max}^{(l)}$ are evaluated in between the structures in the cross-shore street. The increase in the maximum water levels and a marginal increase in the maximum cross-shore velocity (Figure 17) led to a noticeable increase of the maximum momentum flux inside the streets of the building array in the first rows when comparing the maximum momentum flux to bare earth values. Critical infrastructure in areas where flow constriction can happen should be carefully analyzed due to the potential increase of maximum inundation levels and momentum fluxes. However when n > 8, MRF < 1, meaning that after about 8 rows inland, the maximum momentum flux starts to be lower than the maximum bare earth momentum flux. This is explained by the combined reduction on RRF and VRF when n > 8. An upper envelope for MRF is presented in equation (23).

$$MRF_{env} = \frac{1.84}{(1 + 0.20 \cdot n)^{0.701}}$$
 (23)

A similar monotonic decrease of the maximum flux in a cross shore street depending on the distance to the shoreline has been previously observed in physical tsunami experiments of the city of Seaside, OR (Shin et al., 2012).

From the increase in (1) the maximum free surface elevation, (2) the maximum velocity, and (3) the maximum momentum flux in the cross-shore street, it seems that the reduction in the wave loads on the sheltered structures is given by the deflection of the flow through the cross-shore street channel. This effect should be considered to estimate possible loads by external elements travelling through cross-shore streets, such as floating debris that could impact against the structures further inland. Although the impact on structures from debris is beyond the scope of this study, it should not be neglected. As investigated by Hatzikyriakou et al. (2016), structures surrounded by other structures are more likely to remain structurally intact, but they are more likely to have partial damage from debris belonging to the more exposed structures.

7. Conclusions

This paper analyzes the effect of a building array on maximum run-up wave loading. The analysis was conducted through the use laboratory experiments and Computational Fluid Dynamics (CFD) simulations. The key points of this paper are presented as follows:

- Under the wave conditions and the geometry tested, maximum wave run-up loads decrease as more rows of buildings are providing shelter. Monotonically decreasing Load Reduction Factors (LRF) are defined to evaluate the magnitude of the load reduction. For both the unbroken and the broken wave conditions tested, when 4 or more rows are providing shelter, Load Reduction Factors are less than 1/4, with most of the reduction taking place in rows 1 to 4. The rate of sheltering, given by the slope of LRF envelopes, was also found to be monotonically decreasing with the number of rows providing shelter.
- The reduction of maximum values of wave loading are very sensitive to the effect of blocking ratio w^* , relative clearance distance d^* , and relative offset o^* , indicating that additional tests should be conducted to draw more general conclusions regarding the effect of w^* , d^* , and o^* on the reduction of maximum wave loads.
- Maximum inundation levels, cross-shore velocity, and cross-shore momentum flux values in the cross-shore streets were up to 2.6, 1.2, and 1.8 times higher than maximum bare earth values, respectively. These values decrease as more rows providing shelter are considered, reaching bare earth levels when about 8 rows are considered. This shows that the drawback of providing shelter to the structures is the increase in the magnitude of the hydrodynamics in the cross-shore streets, at least in the first 8 rows. Given that most of the operational models assume a bare earth condition, these findings should not be neglected because hydrodynamics levels inside a building array could be considerably higher than values estimated by bare earth models.
- Considering that it is common to estimate unobstructed maximum wave loading using maximum values of bare earth momentum flux, we found that for the unbroken wave condition unobstructed maximum loads were reasonably estimated with the maximum bare earth momentum flux. However, for the broken wave condition the maximum momentum flux in some cases underestimates the maximum wave loading.
- There are several limitations in this study, such as the structures size, spacing distances, beach slope, and wave conditions. This study assumes that no debris are present and that all the structures remains in place when the inundation event happens. The conclusions drawn from this study are valid for our limited cases and additional tests have to be conducted to extend our findings to more general conclusions.

Declaration of competing interest

The authors declare that they have no known competing financial interests or personal relationships that could have appeared to influence the work reported in this paper.

Acknowledgements

Funding for this work was provided by National Science Foundation grants 1661015, 1727662, and a National Institute of Standards and Technology grant. Their support is gratefully acknowledged. The authors would like to express their gratitude to Adam Keen, Pedro Lomonaco, Tim Maddux, Sean Duncan, Hyoungsu Park, Takuya Miyashita, Ezgi Çinar, Tori Tomiczek, and the

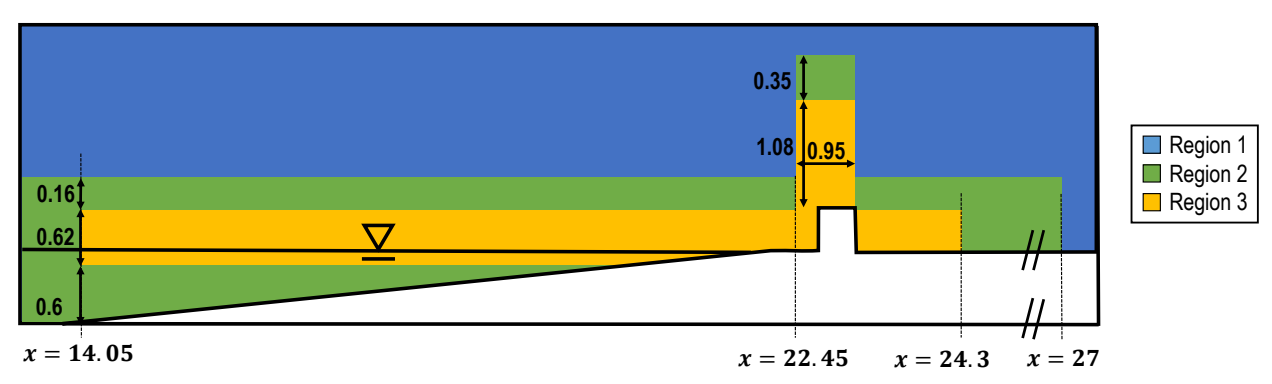


Figure A1: Different meshing regions used in the simulations of the Kyoto Experiments. Regions 1 and 2 in left-most part of the figure extend until the location of the wavemaker at x = 0. Dimensions are in meters.

staff of the O.H. Hinsdale Wave Research Laboratory for their help with the laboratory experiments. The authors also thank the comments of the anonymous reviewer that significantly helped to clarify and improve this manuscript.

A. Description of the different meshes used in the validation

As mentioned in the validation in section 3, three different meshes were tested until good agreement with the experimental data was achieved. Key meshing regions were defined for both the simulation of the Kyoto Experiment performed by Tomiczek et al. (2016) and, as a part of this study, the OSU Experiment (Figures A1 and A2). In general, higher resolution was placed in the following regions: at the water-air interface, high flow acceleration areas, wave breaking location, over the test bed, and around the structures. The resolution used in each region is presented in a compacted and dimensionless grid length Δs^* defined in equation (24)

$$\Delta s^* = \frac{\sqrt{\Delta x^2 + \Delta y^2 + \Delta z^2}}{\sqrt{w_x^2 + w_y^2 + w_z^2}}$$
 (24)

where Δx , Δy , and Δz are the resolution in the cross-shore, along-shore and vertical directions, respectively. w_x , w_y , and w_z are the structure dimensions in the x, y, z directions, respectively. Information regarding the simulations are presented in Table A.1. To keep simulations stable, CFL was kept below 0.5. This restriction leads to very high computation time for small values of Δs^* . For instance, the fine mesh for the Kyoto and OSU Experiments have a similar number of cells implemented on a similar number of computing cores, however the computation time for the OSU case is almost three times as much as for the Kyoto case. The difference in computation time is explained by the reduction in the timestep Δt in the OSU case to keep the simulation stable (CFL = $\Delta t \sum_{i=1}^3 u_i/\Delta x_i < 0.5$). We attempted to reduce the computation time by increasing the number of computer cores, but we experienced poor parallel efficiency on the fine mesh which led us to prefer running multiple simulations with 96 to 120 computational cores at the same time rather than running a few simulations using a large number of computational cores.

Figures A3, A4 present the agreement between the experimental data and the simulations of the offshore free surface elevation and the onshore free surface elevation, respectively. There is a

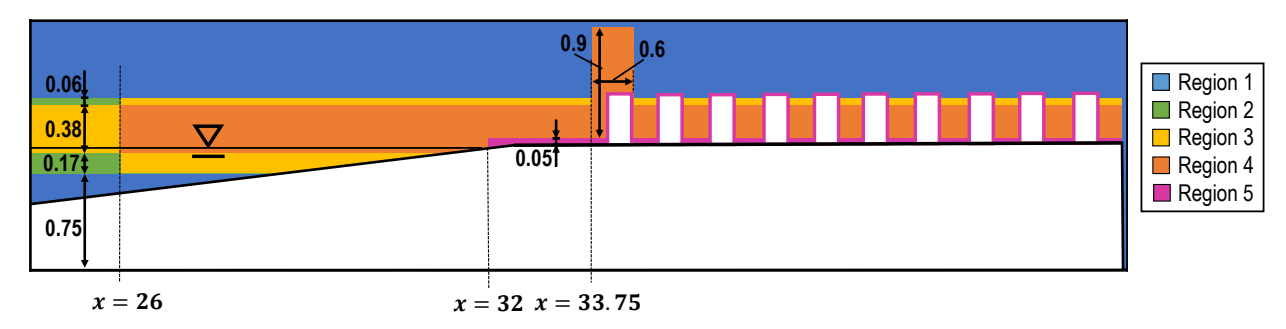


Figure A2: Different meshing regions used in the simulations of the OSU Experiment. Regions 1, 2, and 3 in left-most part of the figure extend until the location of the wavemaker at x = 0. A 0.02 m Region 5 layer is placed in the surrounding of the structures. Dimensions are in meters.

Table A.1 Simulation details of the coarse, mid and fine meshes for both the Kyoto and the OSU Experiment. n_{cells} is the number of cells in the domain, n_{cores} is the number of cores used in the simulation run.

Simulation details of the Kyoto Experiment							
		Δ s *		0/1			
Mesh	Region 1	Region 2	Region 3	n_{cells}	n_{cores}	Computation time (d)	
Coarse	0.367	0.0918	0.0918	724,564	120	0.2	
Mid	0.367	0.0459	0.0459	5,047,981	120	1.0	
Fine	0.367	0.0459	0.0229	19,251,937	120	3.5	

Simulation details of the OSU Experiment

		Δ s *						
Mesh	Region 1	Region 2	Region 3	Region 4	Region 5	n_{cells}	$n_{\rm cores}$	Computation time (d)
Coarse	0.924	0.115	0.0577	0.0577	0.0577	2,639,530	96	0.7
Mid	0.924	0.115	0.0577	0.0289	0.0289	11,615,441	96	3.8
Fine	0.924	0.115	0.0577	0.0289	0.0144	17,270,747	96	10.2

good agreement with the experimental data and the numerical results in the offshore region with no differences between the coarse, mid, and fine mesh because, as presented in Table A.1, Δs^* remains unchanged in the offshore region. In the offshore region we can show good agreement with the experimental data, but we cannot ensure convergence because Δs^* had the same value in the three meshes presented in this work. The simulated onshore free surface elevation in the cross-shore center channel (USWG1, USWG3, USWG5, USWG7, USWG9, and USWG10) shows good agreement with the experimental data regardless the mesh used, yet the free surface elevation at the front of the structures (USWG2, USWG4, USWG6, and USWG8) shows differences. The simulated η at the location of USWG2 does not have a considerable difference between the three different meshes reaching a maximum value of $\eta_{max} = 0.25$ m, whereas the experimental η_{max} is much larger. This may be explained by the difference of how the free surface elevation is measured in the laboratory and how η is computed in the simulation. The USWGs measure the closest body of

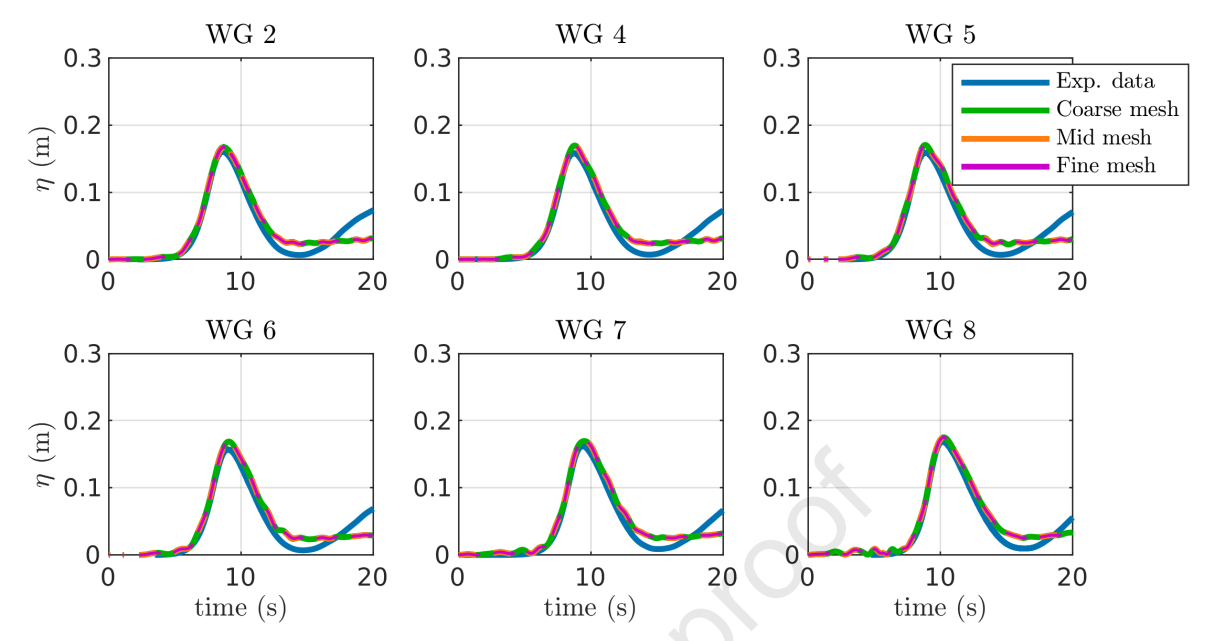


Figure A3: Free surface elevation comparison of the offshore WG between the OSU experimental data and the simulations with the three different mesh resolutions

water from the top, that could result in high values of η due to water splashing. In the simulations, η is obtained by vertically integrating the fraction of water α as $\int_0^\infty \alpha dz$, which neglects splashing in any disconnected column of water.

Figure A5 shows the agreement between the experimental and the simulated onshore horizontal velocity. Unfortunately there are experimental data gaps from the ADVs because the device did not record data when a mix of water and air was present. The cross-shore velocity results did not present significant difference with between the three meshes, indicating a fairly good agreement with the available data points.

CRediT authorship contribution statement

Joaquin P. Moris: Conceptualization, Methodology, Software, Validation, Formal analysis, Investigation, Writing - Original Draft, Visualization. **Andrew B. Kennedy:** Conceptualization, Methodology, Investigation, Resources, Writing - Review Editing, Supervision, Project administration, Funding acquisition. **Joannes J. Westerink:** Conceptualization, Resources, Writing - Review Editing, Supervision.

References

Angel, S., Parent, J., Civco, D.L., Blei, A., Potere, D., 2011. The dimensions of global urban expansion: Estimates and projections for all countries, 2000–2050. Progress in Planning 75, 53–107.

Arabi, M.G., Sogut, D.V., Khosronejad, A., Yalciner, A.C., Farhadzadeh, A., 2019. A numerical and experimental study of local hydrodynamics due to interactions between a solitary wave and an impervious structure. Coastal Engineering 147, 43–62.

Ardianti, A., Mutsuda, H., Doi, Y., 2015. 2015a-gs19-3 interactions between run-up tsunami and structures using particle based method, in: Conference Proceedings The Japan Society of Naval Architects and Ocean Engineers 21, The Japan Society of Naval Architects and Ocean Engineers. pp. 623–628.

ASCE7-16, 2017. Minimum design loads and associated criteria for buildings and other structures.

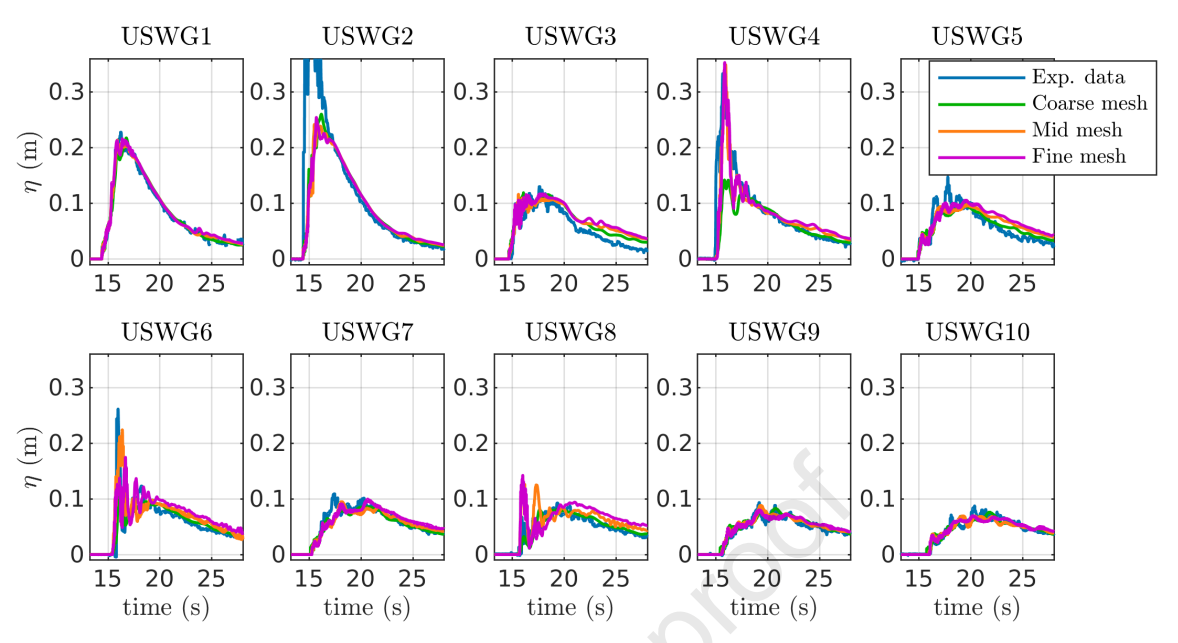


Figure A4: Free surface elevation comparison of the onshore WG between the OSU experimental data and the simulations with the three different mesh resolutions

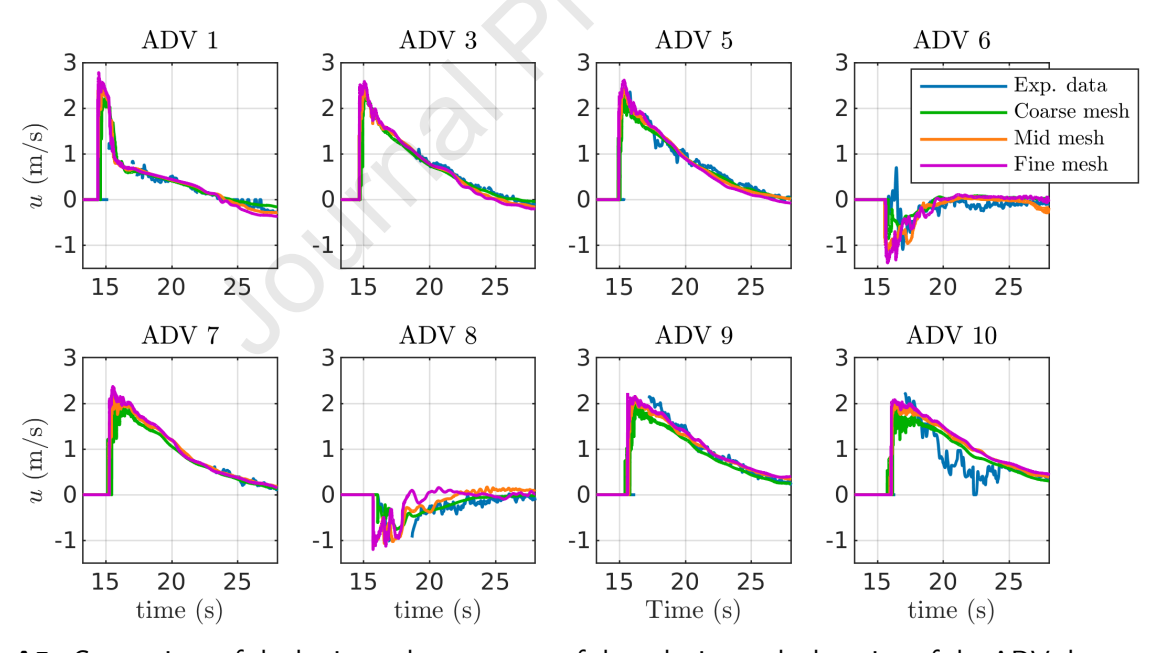


Figure A5: Comparison of the horizontal component of the velocity at the location of the ADVs between the OSU experimental data and the simulations with the three different mesh resolutions

Athukorala, P.c., Resosudarmo, B.P., 2005. The indian ocean tsunami: Economic impact, disaster management, and lessons. Asian economic papers 4, 1–39.

Brackbill, J., Kothe, D.B., Zemach, C., 1992. A continuum method for modeling surface tension. Journal of computational physics 100, 335–354. Bullock, G., Obhrai, C., Peregrine, D., Bredmose, H., 2007. Violent breaking wave impacts. part 1: Results from large-scale regular wave tests on vertical and sloping walls. Coastal Engineering 54, 602–617.

CCH, 2000. City and county of honolulu building code (cch).

- Chan, E.S., Cheong, H.F., Tan, B.C., 1995. Laboratory study of plunging wave impacts on vertical cylinders. Coastal Engineering 25, 87-107.
- Cuomo, G., Allsop, W., Bruce, T., Pearson, J., 2010. Breaking wave loads at vertical seawalls and breakwaters. Coastal Engineering 57, 424-439.
- Dall'Osso, F., Dominey-Howes, D., Tarbotton, C., Summerhayes, S., Withycombe, G., 2016. Revision and improvement of the ptva-3 model for assessing tsunami building vulnerability using "international expert judgment": introducing the ptva-4 model. Natural Hazards 83, 1229–1256.
- Dall'Osso, F., Gonella, M., Gabbianelli, G., Withycombe, G., Dominey-Howes, D., 2009. A revised (ptva) model for assessing the vulnerability of buildings to tsunami damage. Natural Hazards & Earth System Sciences 9.
- Dall'Osso, F., Maramai, A., Graziani, L., Brizuela, B., Cavalletti, A., Gonella, M., Tinti, S., et al., 2010. Applying and validating the ptva-3 model at the aeolian islands, italy: assessment of the vulnerability of buildings to tsunamis. Nat. Hazards Earth Syst. Sci. .
- Davis, C., Keilis-Borok, V., Kossobokov, V., Soloviev, A., 2012. Advance prediction of the march 11, 2011 great east japan earthquake: A missed opportunity for disaster preparedness. International Journal of Disaster Risk Reduction 1, 17–32.
- Douglas, S., Nistor, I., 2015. On the effect of bed condition on the development of tsunami-induced loading on structures using openfoam. Natural Hazards 76, 1335–1356.
- FEMA, 2011. Fema p-55, coastal construction manual: Principles and practices of planning, siting, designing, constructing, and maintaining residential buildings in coastal areas.
- FEMA, 2012. Fema p-646, guidelines for design of structures for vertical evacuation from tsunamis.
- Fraser, S., Raby, A., Pomonis, A., Goda, K., Chian, S.C., Macabuag, J., Offord, M., Saito, K., Sammonds, P., 2013. Tsunami damage to coastal defences and buildings in the march 11th 2011 m w 9.0 great east japan earthquake and tsunami. Bulletin of earthquake engineering 11, 205–239.
- Fritz, H.M., Petroff, C.M., Catalán, P.A., Cienfuegos, R., Winckler, P., Kalligeris, N., Weiss, R., Barrientos, S.E., Meneses, G., Valderas-Bermejo, C., et al., 2011. Field survey of the 27 february 2010 chile tsunami. Pure and Applied Geophysics 168, 1989–2010.
- Fukuyama, H., Kato, H., Ishihara, T., Tajiri, S., Tani, M., Okuda, Y., Nakano, Y., 2011. Structural design requirement on the tsunami evacuation buildings. UJNR, Tokyo.
- Goda, Y., 1974. New wave pressure formulae for composite breakwaters, in: Coastal Engineering, pp. 1702–1720.
- González-Cao, J., Altomare, C., Crespo, A., Domínguez, J., Gómez-Gesteira, M., Kisacik, D., 2019. On the accuracy of dualsphysics to assess violent collisions with coastal structures. Computers & Fluids 179, 604–612.
- Goseberg, N., 2013. Reduction of maximum tsunami run-up due to the interaction with beachfront development–application of single sinusoidal waves. Natural Hazards and Earth System Science 13 (2013), Nr. 11.
- Hattori, M., Arami, A., Yui, T., 1994. Wave impact pressure on vertical walls under breaking waves of various types. Coastal Engineering 22, 79–114.
- Hatzikyriakou, A., Lin, N., Gong, J., Xian, S., Hu, X., Kennedy, A., 2016. Component-based vulnerability analysis for residential structures subjected to storm surge impact from hurricane sandy. Natural Hazards Review 17, 05015005.
- Higuera, P., 2015. Application of computational fluid dynamics to wave action on structures. PhD. Universidade de Cantabria .
- Higuera, P., Lara, J.L., Losada, I.J., 2013. Realistic wave generation and active wave absorption for navier–stokes models: Application to openfoam®. Coastal Engineering 71, 102–118.
- Huang, M., Kennedy, A., Tomiczek, T., Westerink, J., 2018. Solitary wave impacts on vertical and overhanging near-coast structures. Coastal Engineering Journal 60, 356–370.
- Ishiii, H., Takabatake, T., Esteban, M., Hamano, G., Iimura, K., Shibayama, T., 2019. Experimental investigation on the influence of arrangement of buildings on tsunami run-up flow. Coastal Structures 2019, 465–475.
- Izquierdo, T., Fritis, E., Abad, M., 2018. Analysis and validation of the ptva tsunami building vulnerability model using the 2015 chile post-tsunami damage data in coquimbo and la serena cities. Natural Hazards & Earth System Sciences 18.
- Khew, Y.T.J., Jarzebski, M.P., Dyah, F., San Carlos, R., Gu, J., Esteban, M., Aránguiz, R., Akiyama, T., 2015. Assessment of social perception on the contribution of hard-infrastructure for tsunami mitigation to coastal community resilience after the 2010 tsunami: Greater concepcion area, chile. International journal of disaster risk reduction 13, 324–333.
- Kihara, N., Niida, Y., Takabatake, D., Kaida, H., Shibayama, A., Miyagawa, Y., 2015. Large-scale experiments on tsunami-induced pressure on a vertical tide wall. Coastal engineering 99, 46–63.
- Kirkgöz, M., 1995. Breaking wave impact on vertical and sloping coastal structures. Ocean Engineering 22, 35-48.
- Klammer, P., Kortenhaus, A., Oumeraci, H., 1996. Wave impact loading of vertical face structures for dynamic stability analysis-prediction formulae, in: Coastal Engineering 1996, pp. 2534–2547.
- Ko, H.T.S., Yeh, H., 2018. On the splash-up of tsunami bore impact. Coastal engineering 131, 1-11.
- Kopp, R.E., Horton, R.M., Little, C.M., Mitrovica, J.X., Oppenheimer, M., Rasmussen, D., Strauss, B.H., Tebaldi, C., 2014. Probabilistic 21st and 22nd century sea-level projections at a global network of tide-gauge sites. Earth's future 2, 383–406.
- Larsen, B.E., Fuhrman, D.R., 2018. On the over-production of turbulence beneath surface waves in reynolds-averaged navier-stokes models. J. Fluid Mech 853, 419-460.
- Launder, B., Spalding, D., 1974. The numerical computation of turbulent flow. Comp. Methods Appl. Mech. Eng. 3, 269.
- Leone, F., Lavigne, F., Paris, R., Denain, J.C., Vinet, F., 2011. A spatial analysis of the december 26th, 2004 tsunami-induced damages: Lessons learned for a better risk assessment integrating buildings vulnerability. Applied Geography 31, 363–375.
- Linton, D., Gupta, R., Cox, D., van de Lindt, J., Oshnack, M.E., Clauson, M., 2013. Evaluation of tsunami loads on wood-frame walls at full scale. Journal of Structural Engineering 139, 1318–1325.
- Lugni, C., Brocchini, M., Faltinsen, O., 2006. Wave impact loads: The role of the flip-through. Physics of fluids 18, 122101.
- Lynett, P., Liu, P., Sitanggang, K., Kim, D., 2002. Modeling wave generation, evolution, and interaction with depth-integrated, dispersive wave equations coulwave code manual. Cornell University Long and Intermediate Wave Modeling Package.
- Lynett, P.J., Borrero, J.C., Liu, P.L.F., Synolakis, C.E., 2003. Field survey and numerical simulations: A review of the 1998 papua new guinea tsunami, in: Landslide Tsunamis: Recent Findings and Research Directions. Springer, pp. 2119–2146.
- McGranahan, G., Balk, D., Anderson, B., 2007. The rising tide: assessing the risks of climate change and human settlements in low elevation

- coastal zones. Environment and urbanization 19, 17-37.
- Menter, F.R., Kuntz, M., Langtry, R., 2003. Ten years of industrial experience with the sst turbulence model. Turbulence, heat and mass transfer 4, 625–632.
- Moon, W.C., Chiew, L.Q., Cheong, K.W., Tee, Y.C., Chun, J.B., Lau, T.L., 2019. An experimental study for estimating tsunami wave forces acting on building with seaward and landward macroroughness. Ocean Engineering 186, 106116.
- Nakamura, T., Mizutani, N., Fujima, K., 2010. Three-dimensional numerical analysis on deformation of run-up tsunami and tsunami force acting on square structures, in: Proc. 32nd Int. Conf. on Coastal Eng, ASCE, pp. 14–10.
- Nicolsky, D., Suleimani, E., Hansen, R., 2011. Validation and verification of a numerical model for tsunami propagation and runup. Pure and Applied Geophysics 168, 1199–1222.
- Nouri, Y., Nistor, I., Palermo, D., Cornett, A., 2010. Experimental investigation of tsunami impact on free standing structures. Coastal Engineering Journal 52, 43–70.
- Omira, R., Baptista, M.A., Miranda, J.M., Toto, E., Catita, C., Catalao, J., 2010. Tsunami vulnerability assessment of casablanca-morocco using numerical modelling and gis tools. Natural hazards 54, 75–95.
- Oumeraci, H., Klammer, P., Partenscky, H., 1993. Classification of breaking wave loads on vertical structures. Journal of waterway, port, coastal, and ocean engineering 119, 381–397.
- Park, H., Cox, D.T., Lynett, P.J., Wiebe, D.M., Shin, S., 2013. Tsunami inundation modeling in constructed environments: A physical and numerical comparison of free-surface elevation, velocity, and momentum flux. Coastal Engineering 79, 9–21.
- Park, H., Cox, D.T., Shin, S., 2019. Physical modeling of horizontal and vertical tsunami forces on the elevated overland structure. Journal of Coastal Research 91, 51–55.
- Park, H., Do, T., Tomiczek, T., Cox, D.T., van de Lindt, J.W., 2018. Numerical modeling of non-breaking, impulsive breaking, and broken wave interaction with elevated coastal structures: Laboratory validation and inter-model comparisons. Ocean Engineering 158, 78–98.
- Ramsden, J.D., 1996. Forces on a vertical wall due to long waves, bores, and dry-bed surges. Journal of waterway, port, coastal, and ocean engineering 122, 134–141.
- Reese, S., Bradley, B.A., Bind, J., Smart, G., Power, W., Sturman, J., 2011. Empirical building fragilities from observed damage in the 2009 south pacific tsunami. Earth-Science Reviews 107, 156–173.
- Reese, S., Cousins, W., Power, W., Palmer, N., Tejakusuma, I., Nugrahadi, S., 2007. Tsunami vulnerability of buildings and people in south java. field observations after the july 2006 java tsunami. Natural Hazards and Earth System Sciences, 573–589.
- Robertson, I., Paczkowski, K., Riggs, H., Mohamed, A., 2013. Experimental investigation of tsunami bore forces on vertical walls. Journal of Offshore Mechanics and Arctic Engineering 135.
- Rueben, M., Holman, R., Cox, D., Shin, S., Killian, J., Stanley, J., 2011. Optical measurements of tsunami inundation through an urban waterfront modeled in a large-scale laboratory basin. Coastal Engineering 58, 229–238.
- Rusche, H., 2002. Computational fluid dynamics of dispersed two-phase flows at high phase fractions phd thesis imperial college of science technology and medicine.
- Shafiei, S., Melville, B.W., Shamseldin, A.Y., 2016. Experimental investigation of tsunami bore impact force and pressure on a square prism. Coastal Engineering 110, 1–16.
- Shin, S., Lee, K.H., Park, H., Cox, D.T., Kim, K., 2012. Influence of a infrastructure on tsunami inundation in a coastal city: laboratory experiment and numerical simulation. Coastal Engineering Proceedings, 8–8.
- Simamora, C., Shigihara, Y., Fujima, K., 2007. Experimental study on tsunami forces acting on structures, in: Proceedings of Coastal Engineering, JSCE, Japan Society of Civil Engineers. pp. 831–835.
- Sogut, E., Sogut, D.V., Farhadzadeh, A., 2019. Effects of building arrangement on flow and pressure fields generated by a solitary wave interacting with developed coasts. Advances in Water Resources 134, 103450.
- Suppasri, A., Koshimura, S., Imai, K., Mas, E., Gokon, H., Muhari, A., Imamura, F., 2012. Damage characteristic and field survey of the 2011 great east japan tsunami in miyagi prefecture. Coastal Engineering Journal 54, 1250005–1.
- Thomas, S., Killian, J., Bridges, K., 2015. Influence of macroroughness on tsunami loading of coastal structures. Journal of Waterway, Port, Coastal, and Ocean Engineering 141, 04014028.
- Tomiczek, T., Kennedy, A., Zhang, Y., Owensby, M., Hope, M.E., Lin, N., Flory, A., 2017. Hurricane damage classification methodology and fragility functions derived from hurricane sandy's effects in coastal new jersey. Journal of Waterway, Port, Coastal, and Ocean Engineering 143, 04017027.
- Tomiczek, T., Prasetyo, A., Mori, N., Yasuda, T., Kennedy, A., 2016. Physical modelling of tsunami onshore propagation, peak pressures, and shielding effects in an urban building array. Coastal Engineering 117, 97–112.
- Versteeg, H.K., Malalasekera, W., 2007. An introduction to computational fluid dynamics: the finite volume method. Pearson Education.
- Winter, A.O., Alam, M.S., Shekhar, K., Motley, M.R., Eberhard, M.O., Barbosa, A.R., Lomonaco, P., Arduino, P., Cox, D.T., 2020. Tsunamilike wave forces on an elevated coastal structure: Effects of flow shielding and channeling. Journal of Waterway, Port, Coastal, and Ocean Engineering 146, 04020021.
- Xie, P., Chu, V.H., 2019. The forces of tsunami waves on a vertical wall and on a structure of finite width. Coastal Engineering 149, 65-80.
- Yang, W., Wen, Z., Li, F., Li, Q., 2018. Study on tsunami force mitigation of the rear house protected by the front house. Ocean Engineering 159, 268–279
- Yeh, H., 2006. Maximum fluid forces in the tsunami runup zone. Journal of waterway, port, coastal, and ocean engineering 132, 496-500.

Highlights

Wave run-up load reduction inside a building array

Joaquin P. Moris, Andrew B. Kennedy, Joannes J. Westerink

- The effect of a building array on maximum run-up loads was studied.
- Maximum wave run-up loads decrease as more rows of buildings are providing shelter.
- Load Reduction Factors (LRF) are defined to evaluate the run-up load reduction.
- The inundation depth, velocity, and momentum flux magnitudes inside the building array are larger than bare earth values.

Declaration of interests

☑ The authors declare that they have no known competing financial interests or personal relationships that could have appeared to influence the work reported in this paper.						
□The authors declare the following financial interests/personal relationships which may be considered as potential competing interests:						